Geophysical Journal International

Geophys. J. Int. (2024) **236,** 547–564
Advance Access publication 2023 October 17
GJI Seismology

https://doi.org/10.1093/gji/ggad408

Seismic attenuation tomography of Eastern Europe from ambient seismic noise analysis

F. Borleanu [1], L. Petrescu [1], A. O. Placinta,[1] F. Magrini [2,3] B. Grecu,[1] M. Radulian[1,4,5] and L. De Siena [2,6]

[1] *National Institute for Earth Physics, Măgurele, Romania. E-mail: felix@infp.ro*
[2] *Institute of Geosciences, Geophysics and Geodynamics, Johannes Gutenberg University, Mainz* D-55128, *Germany*
[3] *Research School of Earth Sciences, Australian National University, Canberra* 2601, *Australia*
[4] *Academy of Romanian Scientists, Bucharest* 050045, *Romania*
[5] *Romanian Academy, Bucharest* 010071, *Romania*
[6] *Dipartimento di Fisica e Astronomia (DIFA), Alma Mater Studiorum Università di Bologna, Bologna* 40129, *Italy*

Accepted 2023 October 7. Received 2023 October 7; in original form 2023 March 27

SUMMARY

The Eastern-Europe region (EER), is a complex geotectonic area that captures part of the Alpine-Himalayan Orogen, the subduction of multiple NeoTethys Branches and part of the East European Craton. It is one of the most exciting geological areas in Europe due to a diversity of tectonic processes acting within it: extensional basin evolution, oceanic subduction, post-collisional volcanism, as well as active crustal deformation associated with the push of the Adria plate or the pull of the actively detaching Vrancea slab. This makes EER an excellent natural laboratory to study the behaviour of the lithosphere–asthenosphere system in a heterogeneous tectonic setting. To investigate the lateral heterogeneity and physical properties of the crust in the EER, we use ambient seismic noise data recorded by the vertical components of broad-band stations that have been operational between 1999 and 2020 in Eastern Europe and surrounding regions. We used this significant amount of data and the latest processing techniques of the ambient seismic noise field based on the continuous wavelet transform to compute cross-correlations between various station pairs, turning every available seismic station into a virtual source. The coda of the interstation cross-correlograms were used to determine coda quality factors (Qc) of Rayleigh waves in four different period ranges (3.0–5.0, 5.0–10.0, 10.0–20.0 and 20.0–30.0 s) and to invert them in the 2-D space, constructing the highest resolution attenuation tomography of the region. Our results reveal high attenuation features throughout the northeast Pannonian region, the Bohemian Massif, the East Carpathians and the Moesian Platform. Nevertheless, our findings do not emphasize a close correlation between the depth of sedimentary basins and attenuation features identified at longer periods. In addition, Qc variations are larger at short periods, indicating higher heterogeneity in the uppermost crust of Eastern Europe. Our findings demonstrate the higher efficiency of noise correlation approaches relative to earthquake data analyses investigating Qc at low frequencies.

Key words: Coda waves; Seismic attenuation; Seismic noise; Crustal structure.

1 INTRODUCTION

Eastern Europe is a complex geotectonic area that encompasses part of the Alpine-Himalayan Orogen, the subduction of multiple NeoTethys Branches and a segment of the East European Craton (EEC, Ustaszewski *et al*. 2008). It is one of the most debated regions of Europe due to a wide range of tectonic processes such as extensional basin evolution, oceanic subduction, post-collisional volcanism and active crustal deformation caused by the dynamic Adria plate and questionable subduction at the Eastern Carpathians bending (Fig. 1a). This controversial area, known as the Vrancea Region (VR, Oncescu & Bonjer 1997; Radulian *et al.* 2000; Ismail-Zadeh *et al.* 2012; Ferrand & Manea 2021; Petrescu *et al.* 2021; Enescu *et al.* 2023), is the primary source of seismic hazard in Eastern Europe, generating strong intermediate-depth earthquakes ($M \geq 7.0$) every century. Moreover, previous studies investigating Vrancea earthquakes revealed anomalous peak ground motion characteristics and asymmetric intensity distributions (Sokolov *et al.* 2008; Văcăreanu *et al.* 2015; Constantin *et al.* 2021; Petrescu *et al.* 2023a).

Seismic attenuation observations complement isotropic seismic velocity tomography, improving our understanding of the composition and structure of the Earth. Attenuation has been exploited as an indication of dynamic processes in the lithosphere, as it is more sensitive to minor variations in lithospheric characteristics, such as fluid content, grain size, fault distribution or melts than seismic velocity (Sato *et al.* 2012; Magrini *et al.* 2021; Di Martino *et al.* 2022; King *et al.* 2023). Furthermore, a comprehensive image of the attenuation structures has a significant impact on modelling of tectonic process evolution, seismic hazard assessment, risk reduction and energy exploration industry (De Siena *et al.* 2014; Napolitano *et al.* 2020; Gabrielli *et al.* 2022). Consequently, seismic attenuation algorithms have been continuously updated (Aki 1980; Frankel *et al.* 1990; Takahashi *et al.* 2007; Del Pezzo *et al.* 2016; Sketsiou *et al*. 2020) and are often used to both determine quality factors of various waves (Qp, Qs and Qc) and map their spatial distribution (Yoshimoto *et al.* 1993; Padhy 2009; Borleanu *et al.* 2017; Soergel *et al*. 2020; Napolitano *et al.* 2020). Other studies (Priyono *et al.* 2021), inverted path-averaged attenuation factors (t^*) to provide more reliable attenuation tomographic images. However, using attenuation techniques in areas with complicated geology and sparse station coverage remains a major challenge. Recent studies (Allmark *et al.* 2018; Soergel *et al*. 2020) have proposed using seismic noise to enhance the resolution of seismic attenuation models. The ambient noise contains information about the medium of propagation of waves from a wide range of continuous and simultaneous sources. Moreover, it is considered a valuable tool for creating desired configurations of virtual sources and receivers to satisfy the much-needed input for various processing algorithms.

The study objective is to investigate the lateral heterogeneity and physical properties of the crust in Eastern Europe. To achieve this aim, we use cross-correlations between station pairs that were operational between 1999 and 2020 in the study region (Fig. 1b), to compute the empirical Green's function (EGF) associated with Rayleigh waves in the microseism period range and determine coda quality factors (Qc). We subsequently inverted the path Qc to map seismic attenuation in different period ranges using a modified version of the Multi-Resolution Attenuation Tomography (MuRAT2D, De Siena *et al.* 2017) algorithm, based on the sensitivity kernels proposed by Del Pezzo *et al.* (2016). Our results provide the highest resolution attenuation image of this region, shedding light on how heterogeneous structures influence wave propagation, and giving us crucial constraints on the role of these features in seismic risk analysis.

2 TECTONIC OVERVIEW

The geology of Eastern Europe is highly heterogeneous, reflecting the stepwise growth of a continent from the Archean-Proterozoic formation of the EEC (>0.5 Ga) to the progressive accretion of younger tectonic units at its edges throughout the Phanerozoic (Neubauer 2003). The Teisseyre-Tornquist Zone (TTZ, Fig. 1), stretching from the North Sea to the Black Sea and Anatolia, separates the EEC from the Phanerozoic accreted terranes, characterized by a thinner and warmer lithosphere (Gee & Stephenson 2006; Pharaoh *et al.* 2006; Petrescu *et al.* 2022; Petrescu *et al.* 2023b). The central European lithosphere comprises a mosaic of Gondwana-derived terranes amalgamated during the Caledonian and Variscan orogenies (e.g. Pharaoh 1999; Thybo *et al.* 2002) and subsequently affected by intraplate volcanism and sedimentary-basin development (Meier *et al.* 2016). Although its signatures are recognizable in the northern sector, the TTZ vanishes beneath the Carpathian Orogen (Pharaoh *et al.* 2006; Borleanu *et al.* 2021). The Carpathian–Pannonian Region (CPR) comprises a hyper-extended sedimentary basin surrounded by collisional orogens. The CPR evolved as ALCAPA and Tisza-Dacia tectonic units collided with the Moesian Platform and the EEC throughout the Miocene (Fig. 1, Ciulavu *et al.* 2000; Ren *et al.* 2013; Mațenco *et al.* 2022). Backarc extension in the Pannonian was coeval with orogenic shortening in the Carpathians (e.g. Lorinczi & Houseman 2010) and diverse magmatic activity migrated from west to east across the present-day location of the basin (Pécskay *et al.* 2006; Seghedi *et al.* 2022).

The CPR hosts a range of heterogeneously distributed sedimentary basins with contrasting evolution histories and underlying crustal structures. The Carpathian foreland consists of Neogene-Quaternary sediments deposited over Precambrian crustal units covered with Palaeozoic deposits from previous orogenies. The Focșani Basin, located at the bend of the South-East Carpathians (FB, Fig. 1a) is the thickest Neogene sedimentary basin in the Carpathian Foreland (∼13 km) and is actively subsiding (Tărăpoancă *et al.* 2003; van der Hoeven *et al.* 2005; Bocin *et al.* 2013). The Transylvanian Basin (TB), located on the western side of the Carpathian Orogen (Fig. 1a) is 1–3 km thick and has been deformed and uplifted at different time stages (Huismans *et al.* 1997; Ciulavu 1999). Its tectonic and sedimentary history is markedly different in comparison with most of the intra-Carpathian basins (Krézsek & Filipescu 2005; Tiliță *et al.* 2006), which had a typical backarc-type evolution (e.g. Csontos *et al.* 1992; Tari & Horváth 1995; Bada 1999; Fodor *et al.* 1999). The TB is characterized by a relatively thick continental crust (Visarion & Veliciu 1981; Răileanu *et al.* 1994; Ren *et al.* 2013; Petrescu *et al.* 2019) and regional low surface heat flow (e.g. Demetrescu *et al.* 2001). The TB is separated from the Pannonian Basin by the Apuseni Mountains, a high topography region exposing metamorphic cores of the Tisza and Dacia units and a section of the Vardar oceanic ophiolites (Schmid *et al.* 2008; Mațenco & Radivojević 2012). The Pannonian Basin (Fig. 1a) is a heterogeneous backarc sedimentary basin with thicknesses varying between 1 and 8 km (Horváth *et al.* 2006), sitting on a hyper-extended and warm lithosphere and crust (e.g. Kalmár *et al.* 2021) enclosed by collisional orogens (Horváth *et al.* 2006; Mațenco & Radivojević 2012).

The crust of the CPR has been subject to intensive magmatism in the past ∼20 Ma. Igneous rock types range from exposed to subcropped felsic, intermediate and mafic calc-alkaline volcanic (Pécskay *et al.* 2006). Volcanic formations in the CPR are mostly buried beneath Neogene-Quaternary sediments throughout the Pannonian Basin and the TB, and outcrop in several regions in the Carpathians. The Central Slovakia Volcanic Field (CSVF, Fig. 1a) is a calc-alkaline volcanic formation also known as a complex magnetic anomaly area rich in fluids, located on the inner side of the Western Carpathians and bound by the Bohemian Massif to the NW (Konečný *et al.* 1995; Bektaş 2013). The Călimani–Gurghiu–Harghita (CGH) is an intermediate magmatic arc disposed along the East Carpathians at the eastern edge of the TB (Seghedi *et al.* 2019). In the southern Apuseni Mountains, a section of the Vardar oceanic ophiolite that underlies most of the TB is exposed (Fig. 1, Schmid *et al.* 2008; Mațenco & Radivojević 2012).

The VR (Fig. 1a), an active seismic zone located at the bending of the Eastern Carpathians, plays a crucial role in the geodynamics of the CPR. Although it is far enough from most active collisional boundaries, it generates large intermediate earthquakes ($M > 7$), causing the highest seismic hazard in Eastern Europe (Radulian *et al.* 2000; Petrescu *et al.* 2021; Petrescu *et al.* 2023a). However,

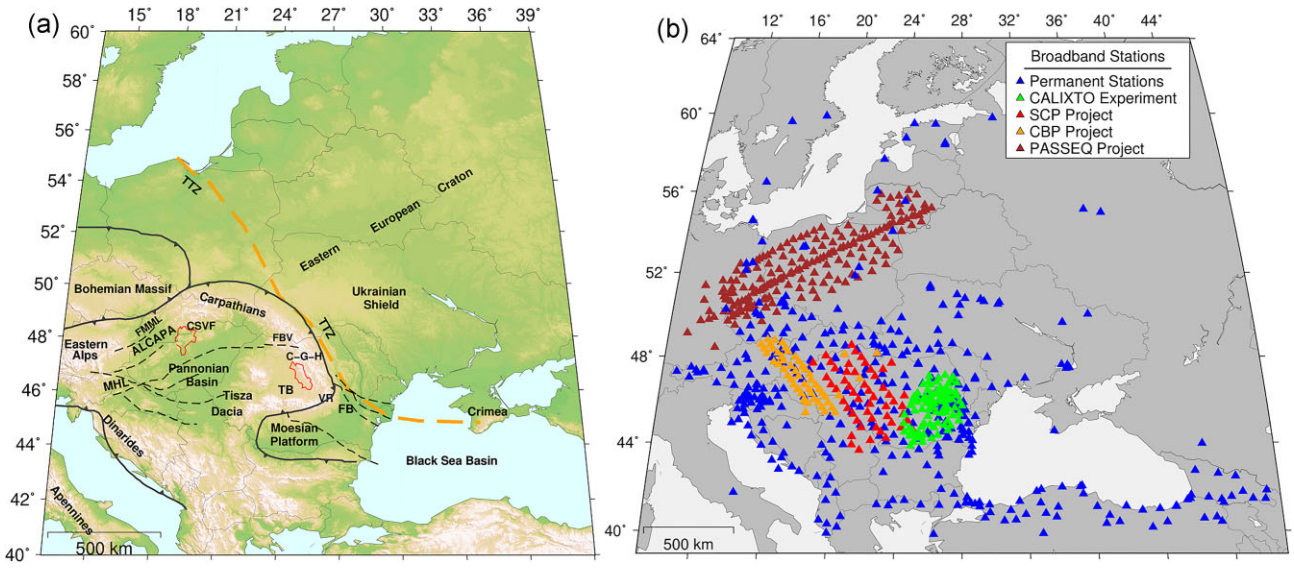

Figure 1. (a) Map showing the main geological and tectonic elements in Eastern Europe and surrounding areas. The orange dashed line outlines the Teisseyre–Tornquist Line (TTZ). The main volcanic structures are shown in red. The black dashed lines indicate major faults that cross-cut the region. (b) Map displaying the permanent and temporary stations used for the current analysis. The abbreviations are as follows: CGH: Călimani–Gurghiu–Harghita; CSVH: Central Slovakian volcanic field; FB: Focșani Basin; FBV: Bogdan Vodă Fault; FMML: Mur-Murz Fault; MHL: Mid-Hungarian Line; TB: Transylvanian Basin and VR: Vrancea region

the link between magmatic activity in CGH and complex processes beneath Vrancea is still highly debated (Ismail-Zadeh *et al.* 2012; Seghedi *et al.* 2019). To the south-east of the Vrancea area, the Focșani Basin hosts moderate-sized crustal seismicity (Radulian *et al.* 2000; Plăcintă *et al.* 2021).

3 PREVIOUS RESEARCH ON SEISMIC ATTENUATION IN EASTERN EUROPE

The current analysis represents the first attempt to examine the characteristics of seismic attenuation on a larger scale in Eastern Europe. Previous research was mainly focused on various areas, pointing out the complexity of the Eastern Europe realm. Herak (1991) used low to moderate crustal earthquakes from the outer Dinarides and the central Adriatic Sea regions. He carried out a quantitative analysis of the frequently observed Qc increase with lapse time for various frequency ranges and showed that Qc increases both with frequency and lapse time, while the degree of frequency dependence decreases with lapse time. Dasović *et al.* (2013) studied the attenuation of coda waves (Qc) from small to moderate earthquakes generated in western continental Croatia. They identified an increasing trend of Qc with lapse time and frequency range, as well as low Qc in the Pannonian basin and higher values for the Dinarides. Kiszely (2000) examined shallow seismic events that occurred in Hungary to determine Qc in the frequency range of 6–24 Hz. He showed an increasing trend of Qc with the frequency range and homogeneous Qc values. Gaebler *et al.* (2015) investigated frequency-dependent seismic scattering and intrinsic attenuation parameters for the crustal structure under West Bohemia using elastic and acoustic radiative transfer theory in a frequency range from 3 to 24 Hz. Strong attenuation patterns were highlighted, with intrinsic attenuation dominating over scattering. Soergel *et al.* (2020) determined and mapped coda-Q in short-to-medium-period ranges (2.5–20 s) in the Alpine region using ambient seismic noise cross-correlations between seismic station pairs. By applying a regionalization approach (Mayor *et al.* 2016) with an adaptive grid (Schaefer *et al.* 2011), they reported high attenuation values in the short-period range (2.5–5 s) in the Po Plain, the Pannonian Basin and the Bohemian Massif. Attenuation studies in the East and South Carpathians include high-frequency waveform modelling (Ardeleanu *et al.* 2022), which indicated low attenuation values in the platform regions surrounding the Eastern Carpathians, in contrast with significant attenuation obtained in the Eastern Carpathians and the Carpathian foredeep. Oancea *et al.* (1991) analysed low to moderate crustal and intermediate-depth earthquakes that occurred across Romania to determine coda quality factors at low frequencies. They build a crustal coda quality factor (Qc) map for Romania, showing a high attenuation regime at the eastern edge of the Pannonian Basin and in the Neogene volcanic area, with low attenuation and strong frequency dependence for the central and eastern parts of Romania. Borleanu *et al.* (2023) used small to moderate crustal earthquakes in Romania to investigate seismic attenuation (in the frequency range of 3–12 Hz) along the Carpathian Orogen. They differentiated the main attenuation mechanisms (scattering and absorption), and mapped them separately, indicating heterogeneous attenuation patterns across the Carpathian sedimentary basins and low seismic attenuation at all frequencies in the EEC.

4 DATA AND METHODS

4.1. Data

Our initial data set consists of vertical component ambient seismic noise records from 734 permanent and temporary broad-band stations that operated between 1999 and 2020 in Central and Eastern Europe (Fig. 1b). Permanent stations belong mostly to national seismic networks operated by countries in our study region, whose data were available for download via the European Integrated Data Archive (EIDA) data services. Temporary networks (Fig. 1b) include the CALIXTO seismic experiment from 1999 (Martin *et al.* 2005), the 2005–2007 Carpathians Basins Project (Dando *et al.* 2011), the 2006–2008 PASSEQ network (Wilde-Piorko *et al.* 2008)

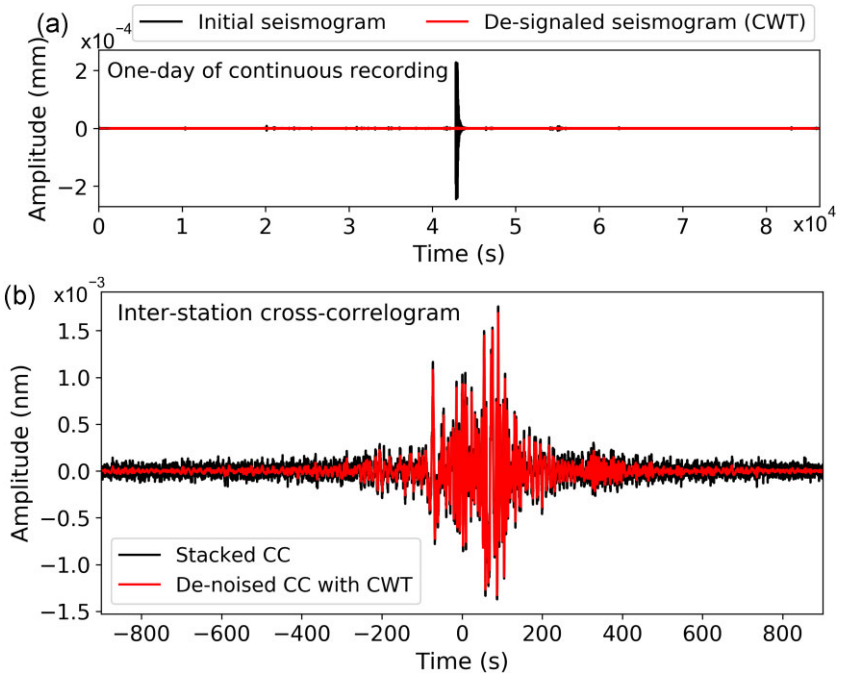

Figure 2. (a) Example of a one-day seismogram from the Tescani (TESR) station in Romania (black trace) and the background noise (red trace) extracted using the CWT (Yang *et al.* 2020) algorithm. (b). Causal and acausal parts of a cross-correlogram between TESR and Voinea (VOIR, Fig. 3), after noise cross-correlation and stacking (black trace), and after de-noising with the CWT (red trace).

and the 2009–2011 South Carpathians Project (Ren *et al.* 2012). To obtain EGFs between stations and Rayleigh wave signals in the microseism period range (4.0–30 s), ambient seismic noise must be recorded simultaneously by pairs of seismic stations. To maximize the number of synchronous station pairs while optimizing data size and processing times, we downloaded data from all available permanent stations operating during the additional temporary deployments, and for the years 2019 and 2020 (Fig. 1b).

4.2. Ambient noise processing in the microseismic frequency range

We decimated the continuous recordings to 5 Hz, removed the mean, detrended, corrected for the instrument response and bandpass filtered them using a Butterworth filter with corner frequencies of 0.003 and 2.4 Hz. We discarded seismograms with time gaps longer than 10 s, or those showing anomalous signal artefacts. One specific difficulty of noise correlations is that they require the handling of transient high-amplitude signals such as earthquakes or long-term amplitude variations (e.g. seasonal). To eliminate such influences, we de-signalled the seismograms using a soft-threshold continuous wavelet transform filter (CWT, Yang *et al.* 2020). This method has been shown to be more efficient than the standard time-domain normalization technique (Bensen *et al.* 2007), by increasing the signal-to-noise ratio (SNR) of Green's functions (Fig. 2) and enhancing the homogeneity of the ambient noise wavefield (e.g. Petrescu *et al.* 2022).

We cut the continuous ambient noise data into 1-hr-long segments in accordance with previous studies that showed that the convergence of correlations occurs faster in shorter time windows than for daily recordings (Poli *et al.* 2012; Soergel *et al.* 2020; Petrescu *et al.* 2022). With the algorithm proposed by Kästle *et al.* (2016), we cross-correlated synchronous noise recordings of 1-hr windows at pairs of stations and stacked the cross-correlograms to obtain interstation EGFs (Fig. 4). Finally, the CWT was used in reverse to de-noise the final cross-correlograms, improving the SNR and highlighting the Rayleigh wave packets (Figs 2 and 3). We visually inspected the data and removed seismograms without high-amplitude dispersive Rayleigh wave packets, resulting in 68 615 waveforms in a distance range of $5 \leq \Delta$ (km) ≤ 3306, showing the highest ray path coverage of this area (Fig. 5).

Fig. 3 and Fig. S1, in the Supporting Information file depict the extracted interstation Rayleigh wave Green's functions computed between VOIR and the stations placed up to 500 km away, showing clear surface wave packets in both causal and acausal cross-correlation sections. We also included examples of Rayleigh wave Green's functions filtered at various period ranges between TESR and VOIR stations, as well as the location of the stations used in the figures below. We can see how microseismic noise affects short-period recordings and how it diminishes over longer periods, resulting in an increase in the SNR.

4.3. Coda quality factor (Qc) determination

Coda quality factors, Qc, were determined based on the Aki & Chouet (1975) approach that estimates the decay of the energy envelope as a function of lapse time (t) measured from the Rayleigh wave arrival (Fig. 4), according to the following equation:

$$A(t, f) = A_0(f)\, t^{-\alpha} e^{\left(-\frac{2\pi f t}{Qc(f)}\right)}, \quad (1)$$

where $A(f,t)$ represents the power spectral density, $A_0(f)$ is a source-dependent term, t is the lapse time measured from the Rayleigh wave arrival, f is the frequency and α is the positive exponent (assumed equal to 1.5, following Calvet *et al.* 2013; Napolitano *et al.* 2020). Qc was determined by a least-squares linear fit of $\log(A(f,t)\, t^{-\alpha})$ versus t for each of the selected period ranges, by applying a modified version of the MuRAT2D algorithm (De Siena *et al.* 2017), initially used for earthquake data processing

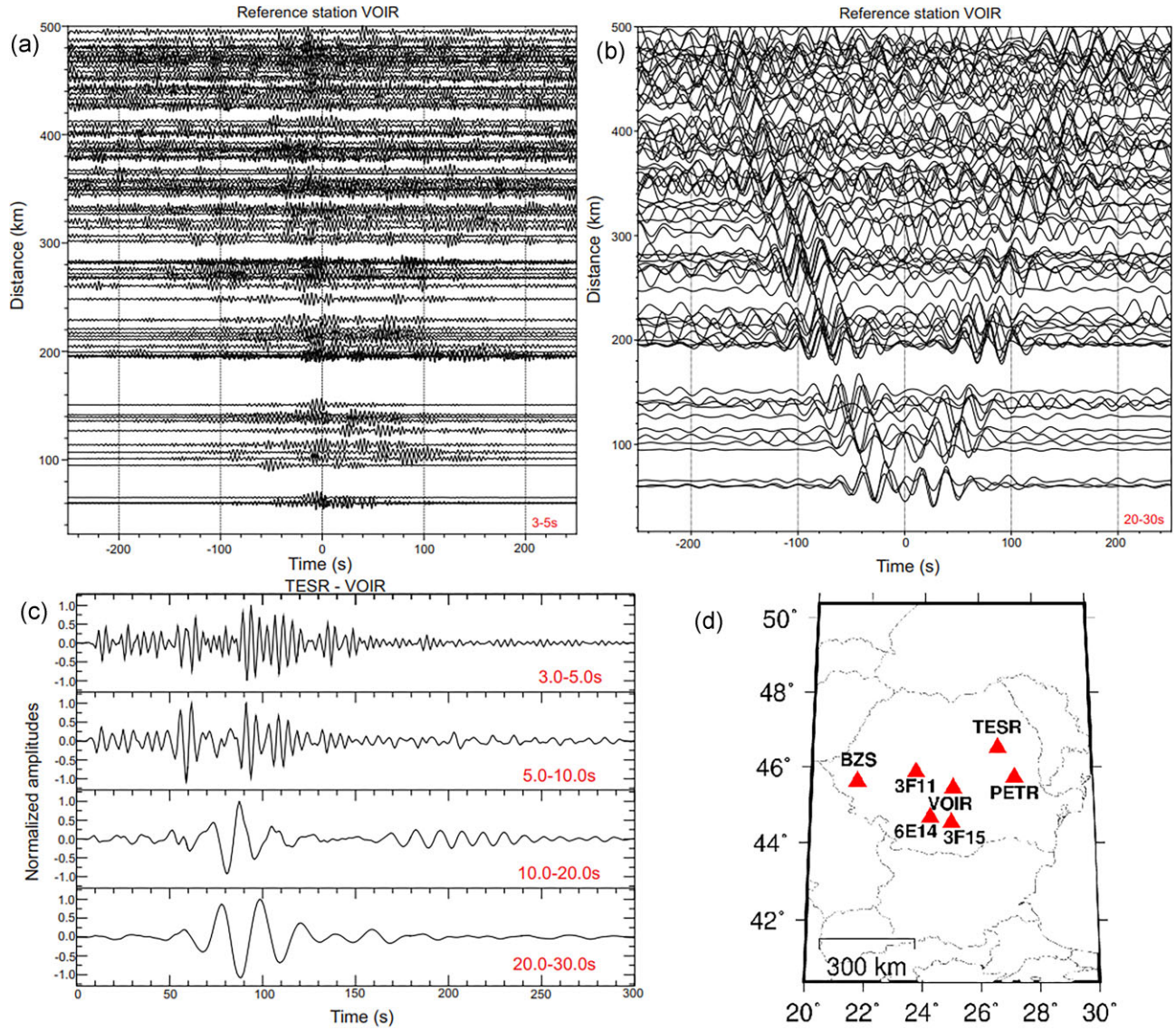

Figure 3. (a) Example of estimated Rayleigh wave Green's functions (acausal and causal sections) in 3–5 s and (b) 20–30 s, for paths between VOIR and the stations, placed up to 500 km away; (c) examples of Green's function of the Rayleigh wave obtained for the station pairs TESR and VOIR, filtered at different period ranges and (d) location of stations used in Figs 3 and 4, and Fig. S2 (Supporting Information).

(Borleanu *et al.* 2017; Sketsiou *et al.* 2020). An example of Qc estimation is given in Fig. S2 (Supporting Information) which shows several EGF's computed for different pairs of stations and their envelopes (bandpass filtered in various period ranges) indicating the decay of the coda waves in time. The algorithm has been adjusted such that the lapse time is measured from the Rayleigh wave arrival instead of the origin time of the seismic event (as it was in the initial version for earthquake analysis). Sato *et al.* (2012) showed that Qc is a sum of the scattering (Qs) and the intrinsic (Qi) quality factors, as in eq. (2).

$$Qc = Qs + Qi \tag{2}$$

where Qs and Qi denote the scattering and intrinsic attenuation (absorption). Recent studies (Calvet & Margerin 2013; Margerin 2017; Napolitano *et al.* 2020; Nardoni *et al.* 2021) showed that at late lapse and no energy leakage from the investigated area, Qc dependence on anisotropy and scattering attenuation decreases significantly, and the Qc can be approximated as a direct measurement of absorption ($Qc = Qi$).

To map stable lateral variations of seismic attenuation, we determined the inverse coda quality factors (Qc^{-1}) in four-period bands (3.0–5.0, 5.0–10, 10.0–20.0 and 20.0–30.0 s). To avoid the possible biases pointed out by the previous research (Calvet *et al.* 2013; Havskov *et al.* 2016; Soergel *et al.* 2020), and to account for the diffusion approximation, we performed multiple trial and error tests to establish the optimum lapse time and coda window length. We tested lapse times between 100 and 150 s and coda window lengths between 400 and 700 s, and inspected the dependence of Qc on traveltimes and whether the output Qc was within a reasonable interval. These criteria were satisfied for a lapse time (lt) of 130 s starting from the arrival of the maximum amplitude Rayleigh wave, and for coda windows (cw) of 400 s for the 3–5 and 5–10 s period intervals, 450 s for 10–20 s, and 700 s for the 20–30 s period interval, respectively (Fig. 4). To show the steps considered for Qc determination, an example of EGF analysis is given in Fig. 4. We show the causal part of a filtered (5.0–10 s) cross-correlogram between

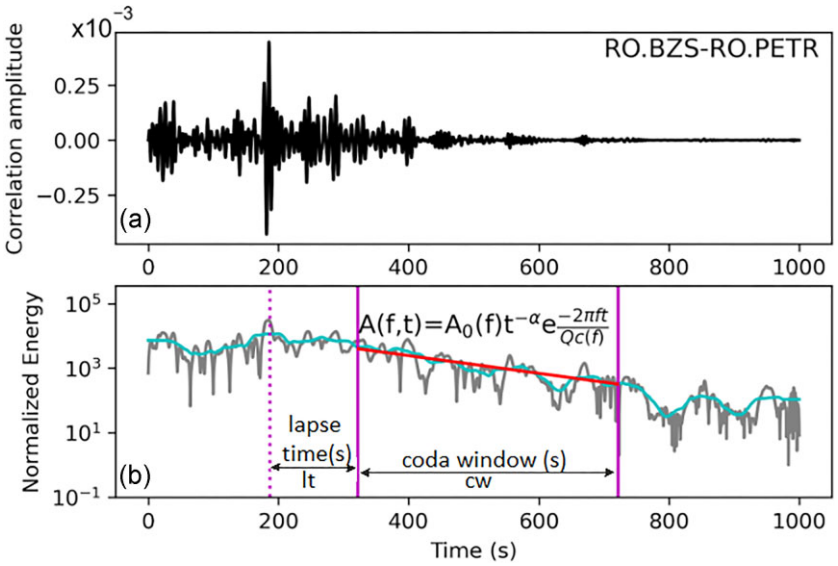

Figure 4. Analysis of a cross-correlogram (EGF) computed between two Romanian stations (BZS and PETR, for an interstation distance of 619 km). (a) Correlation filtered in 5–10 s period range and (b) envelope of the same EGF (grey) and smoothed (cyan). The red line represents the expected coda decay. The solid magenta lines denote the interval boundaries within which the coda is fitted. The onset of the Rayleigh wave is depicted by the magenta dashed line.

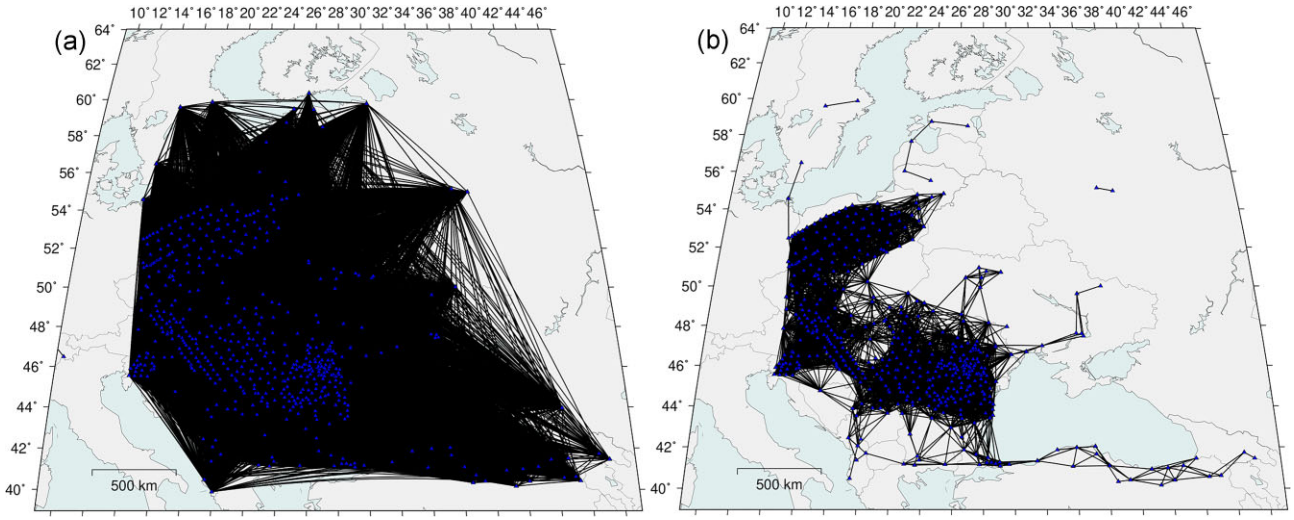

Figure 5. (a) The ray path coverage obtained for the starting data set, comprising EGFs estimated between station pairs with interstation distances of 5–3306 km. (b) Ray coverage corresponding to the data set comprising EGFs between stations with interstation distances ranging from 50 to 250 km, respectively.

Buziaș (BZS) and Petrești (PETR) stations, both located in Romania (Fig. 3), within an interstation distance of 619 km. The Rayleigh wave arrival was estimated as the maximum amplitude measured in a time window corresponding to a velocity interval between 1.5–5.0 km s^{-1} (Soergel *et al.* 2020). The selected lapse time and coda window length are also highlighted in Fig. 4 to justify the chosen parametrization. Figs S3 and S4 in the Supporting Information display the dependency of Qc on backazimuth and Qc^{-1} on the theoretical traveltime, supporting the values selected for lt, cw and interstation distance.

4.4. Data quality control and selection

Soergel *et al.* (2020) indicated that at large interstation distances, Qc has a significant dependence on azimuth, corresponding to the distribution of noise sources. We also computed Qc for various interstation distances and plotted against backazimuth (Fig. S3, Supporting Information) to establish a suitable distance range for the analysis of the selected data. Our results indicate that for interstation distances ranging from 50 to 250 km, the Qc distribution is independent of backazimuth, implying that noise source distribution has a negligible effect on Qc estimations. To justify the selected parametrization for coda waves, in Fig. S3 (Supporting Information), we show the variations of Qc as a function of the backazimuth, for several interstation distances (50–250, 250–500 and 500–1000 km), all computed for the second-period range (5–10 s). The ray path distributions for both initial interstation distances (5–3306 km) and selected ones (50–250 km) are shown in Fig. 5. Fig. S5 (Supporting Information) depicts the distribution of the number of correlations (for 50–250 km) as a function of interstation distance and backazimuth.

In accordance with previous studies (Mayor *et al.* 2016; Soergel *et al.* 2020), we rejected the seismograms for which the coda energy (smoothed over a 40-period window) falls below the noise level corresponding to the analysed window as well as all Qc^{-1} with values smaller than 1×10^{-1} or bigger than 5×10^{-4} measured in the 5–10 and 20–30 s period ranges, respectively higher than 25×10^{-4} in the short-period band (3.0–5.0 s).

To assess the stability of estimated Qc values, before the quality control filters implicit in the MuRAT2D code, we also computed average Qc values for each station, using data from the 50–250 km interstation distance range. We follow Aki & Chouet (1975), estimating the decay of the energy envelope (using eq. 1) of coda Rayleigh waves for each EGF. We then calculated a Qc value for each station by computing the median values of the Qc for cross-correlations that involved that station. The measurements that had values higher than the standard deviation of Qc computed for that station were excluded, while the stations with less than 10 determinations were also excluded from the representation. The resulting Qc values are then compared to the tomographic images obtained using the inversion approach with sensitivity kernels (Del Pezzo *et al.* 2016) described in the next section.

4.5. Spatial sensitivity kernels and Qc inversion

To obtain a forward model for the tomographic inversion in space, all Qc values were weighted across the nodes of a grid with the analytic functions developed by Del Pezzo *et al.* (2016). The authors used the Monte Carlo approach to solve the energy transfer equation, taking into account that repeated anisotropic scatterings cause diffusion in a time span when equipartition occurs and in the absence of leakage and strong boundary limits (Hennino *et al.* 2001; Souriau *et al.* 2011; De Siena *et al.* 2014; Margerin 2017; Napolitano *et al.* 2020). Equipartition is a necessary condition for the onset of diffusion and requires a lack of coherent energy within the coda window chosen for the analysis (Calvet *et al.* 2013). If diffusion can be assessed and leakage is absent, Qc is a direct marker of absorption. Sketsiou *et al.* (2020) provided a comprehensive description of Qc spatial sensitivity functions, also known as sensitivity kernels, which are valid in the diffusive regime.

$$\begin{aligned} \mathrm{F1i,j\,[x,\,y,\,xr,\,yr,\,xs,\,ys,\,\delta x,\,\delta y]} &= \frac{1}{4\pi\,\delta x\,D^2\delta y} \\ &\exp\left[-0.5\frac{\left(x-\frac{x_r+x_s}{2}\right)^2}{2(\delta x\,D)^2}+\frac{\left(y-\frac{y_r+y_s}{2}\right)^2}{0.5(\delta y\,D)^2}\right] \\ &+\frac{1}{2\pi\,\delta x\,D^2\delta y}\exp\left[-0.5\frac{(x-x_s)^2}{2(\delta x\,D)^2}+\frac{(y-y_s)^2}{2(\delta y\,D)^2}\right] \\ &+\frac{1}{2\pi\,\delta x\,D^2\delta y}\exp\left[-0.5\frac{(x-x_r)^2}{2(\delta x\,D)^2}+\frac{(y-y_r)^2}{2(\delta y\,D)^2}\right]. \end{aligned} \tag{3}$$

In eq. (3), F1 is an analytical lapse-time-independent kernel; x_s and y_s, are the source coordinates; x_r and y_r, are the receiver coordinates; δx and δy, are the spatial apertures of the weighting function and D is the horizontal source–receiver distance (Del Pezzo *et al.* 2016; Sketsiou *et al.* 2020).

The kernels shown in eq. (3) are used in the inversion for the spatial distribution of Qc. De Siena *et al.* (2017) defined the elements of the data vector as the source–receiver measurements of Qc^{-1}, gridded the study area, solved eq. (3), and used the results as a sensitivity kernel for a 2-D inversion of Qc^{-1}. In the inversion matrix, the rows of the sensitivity kernels are normalized to their maximum value, meaning that the total coda energy can only be represented by its spatial interaction with the grid (Margerin 2017; Sanborn *et al.* 2017). A zeroth-order Tikhonov regularization is used to solve the corresponding linear inverse problem. The result is a matrix with Qc values for each block of the grid. Inverting the data also helps us to assess the solution's resolution and stability by performing synthetic tests (Rawlinson & Spakman 2016). The tomographic algorithm estimates the damping parameter based on the elbow of the L-curve (Fig. 6), but we assessed the resolution output using multiple algorithms.

In contrast with standard Qc imaging, our method takes into consideration space-weighted functions, which increase the lateral resolution of attenuation (De Siena *et al.* 2017). Sketsiou *et al.* (2020) showed that the use of sensitivity kernels provides a more accurate representation of absorption patterns. The distinction here is that, while a Qc value is computed for each waveform, a larger contribution of the regions around the source and the receiver is taken into account when inverting for the spatial distribution of the absorption anomalies using sensitivity kernels (Del Pezzo *et al.* 2016, Fig. S6, Supporting Information). Space-weighted functions also allow the computation of a forward model (Sketsiou *et al.* 2020), which is further used to conduct synthetic tests (Rawlinson & Spakman 2016) to determine the accuracy and resolution of the resulting models. By applying space-weighted functions, we increased the lateral resolution of the attenuation maps with respect to standard Qc imaging (De Siena *et al.* 2017).

4.6. Mapping strategy and resolution assessment

The study region was divided into cells of $0.68^\circ \times 0.7^\circ$ (X, Y) for discrete period intervals centered on 4.0, 7.5, 15.0 and 25.0 s, respectively. Considering the number of waveforms and their distribution in space, we parametrized the region into a regular grid of 696 cells.

We determine the resolution of our tomography model using classic checkerboard tests (Fig. 6). We create synthetic models of alternating anomalies and invert them with the existing configuration of virtual earthquakes and stations to examine how well the anomaly pattern is reproduced. Checkerboard tests are especially useful for determining the minimum dimension required for an underground structure to be visible using this type of tomography and testing lateral changes in model resolution (Rawlinson *et al.* 2014). We constructed the input model with a cell dimension twice as large as the node spacing and found that the input pattern is properly recovered for all period ranges, with the best solution generated in the 10–20 s period range. In areas with the highest station and ray density (Figs 1, 5 and 6), the input model is well recovered, while the northeast and southwest regions are poorly constrained, where ray coverage is sparse (Figs 5 and 6). The highest resolution region where checkerboard patterns are well recovered is the CPR. The optimum damping value was determined based on the L-curve, a log–log representation of the norm of the regularized solution function versus the norm of the corresponding residual (Hansen & O'Leary 1993). We constructed the L-curve using a wide range of damping values within the elbow range, for which we plotted the corresponding tomographic images. Fig. 6(a) shows selected tomographic images generated for the initial picked damping value range, for the 10–20 s period interval. Visual assessment of the three tomographic images (Fig. 6a) shows that the first two damping values underfit the analysed data and affect the recovery of checkerboard

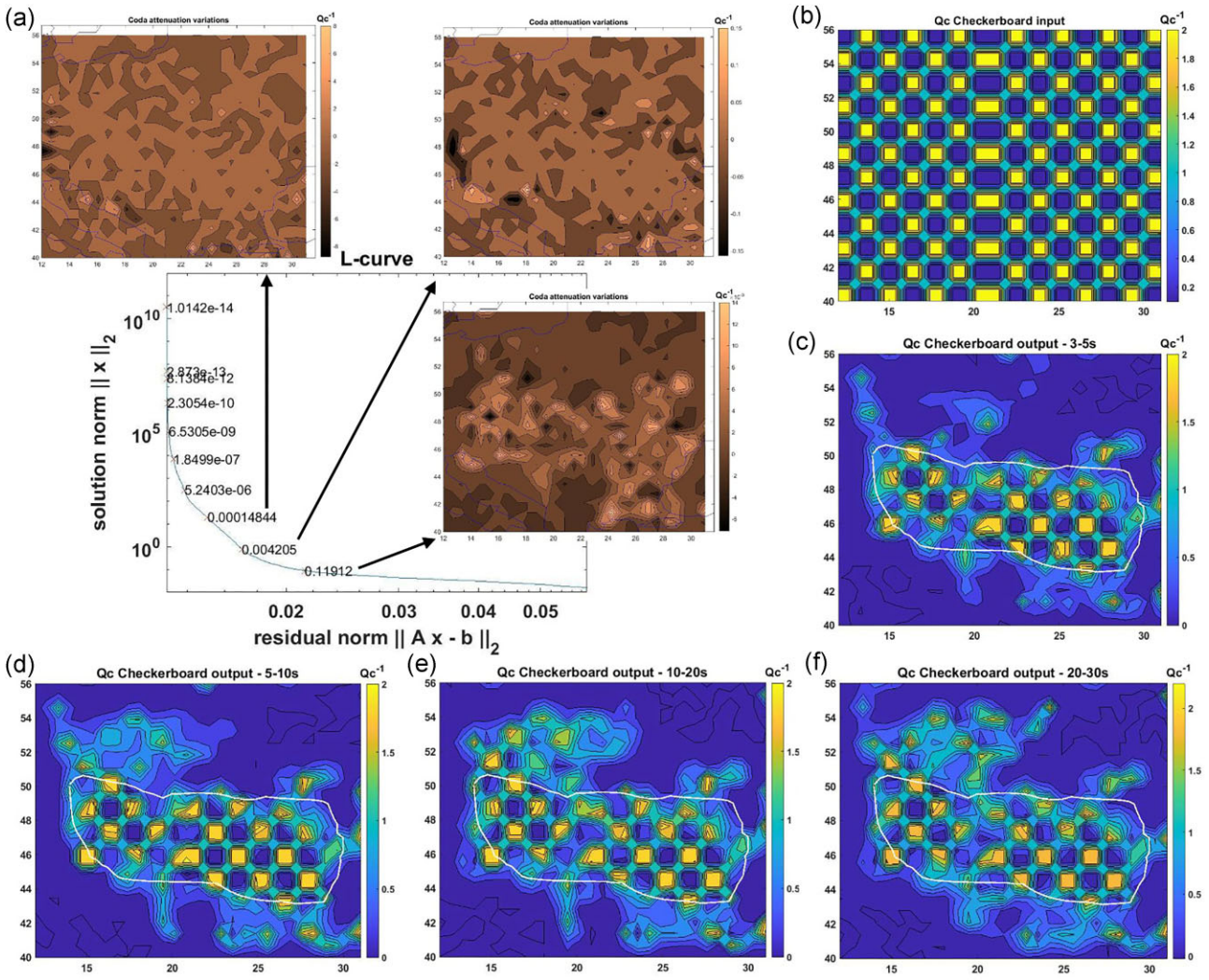

Figure 6. (a) Examples of an *L*-curve graph with Qc^{-1} maps obtained for several elbow values used to estimate the proper damping for the inversion at 15 s (note the change in colour scale); (b) input model showing synthetic checkerboard attenuation anomalies expressed as Qc^{-1} and the corresponding output solutions for: (c) 4.0 s, (d) 7.5 s, (e) 15 s and (f) 25 s. The white line marks the area where our results have the highest resolution.

patterns even in high ray-density areas. Therefore, we considered 0.12 to be the optimum value.

To check for any potential dominant directions of microseismic noise sources that could bias Rayleigh wave propagation, we separately investigated causal and acausal signals and displayed the attenuation variation maps as $(Qc/Qm)^{-1}$ in Fig. 7, where high attenuation structures associated with high absorption features are represented in red, while the low attenuation areas are shown in blue. The slight differences in attenuation patterns could be caused by the various distributions of microseismic noise sources. For seismic stations in Romania, Grecu *et al.* (2012) identified the main microseismic noise sources distributed across the Black Sea, Mediterranean Sea and Atlantic Ocean. This causes the amplitudes of the causal signals to differ from those of the acausal signals (Fig. 3 and Fig. S1, Supporting Information), influencing in some areas the shape or amplitude of the attenuation patterns or even shifting the anomaly (Fig. 7). In accordance with the previous studies (Soergel *et al.* 2020), we further map the attenuation structures using the causal signal.

5 RESULTS

Fig. 8 shows our estimated seismic attenuation models of the CPR, expressed as the inverse of Qc values, scaled by the inverse regional average (Qm^{-1}). The initial Qc^{-1} values were computed by inverting source–receiver Qc^{-1} determinations using the sensitivity kernels approach defined in eq. (3). Qm^{-1} was computed by averaging Qc^{-1} over the whole data set, for each of the selected period ranges, such that it samples different crustal levels depending on the period. Using final ray path coverage (Fig. S7, Supporting Information) and checkerboard pattern recovery tests we marked the area where our model is most stable and well constrained. This area includes the Bohemian Massif, the Easternmost Alps, the Western Carpathians, the Pannonian Basin, the Apuseni Mountains, the TB, the Eastern and South Carpathians, the Eastern Carpathian foreland region of the EEC and the Moesian Platform.

On average, Qc values decrease with increasing period intervals, indicating a frequency-dependent attenuation pattern (Fig. S4, Supporting Information), similar to the results of Soergel *et al.* (2020). Average Qc values for our model vary from

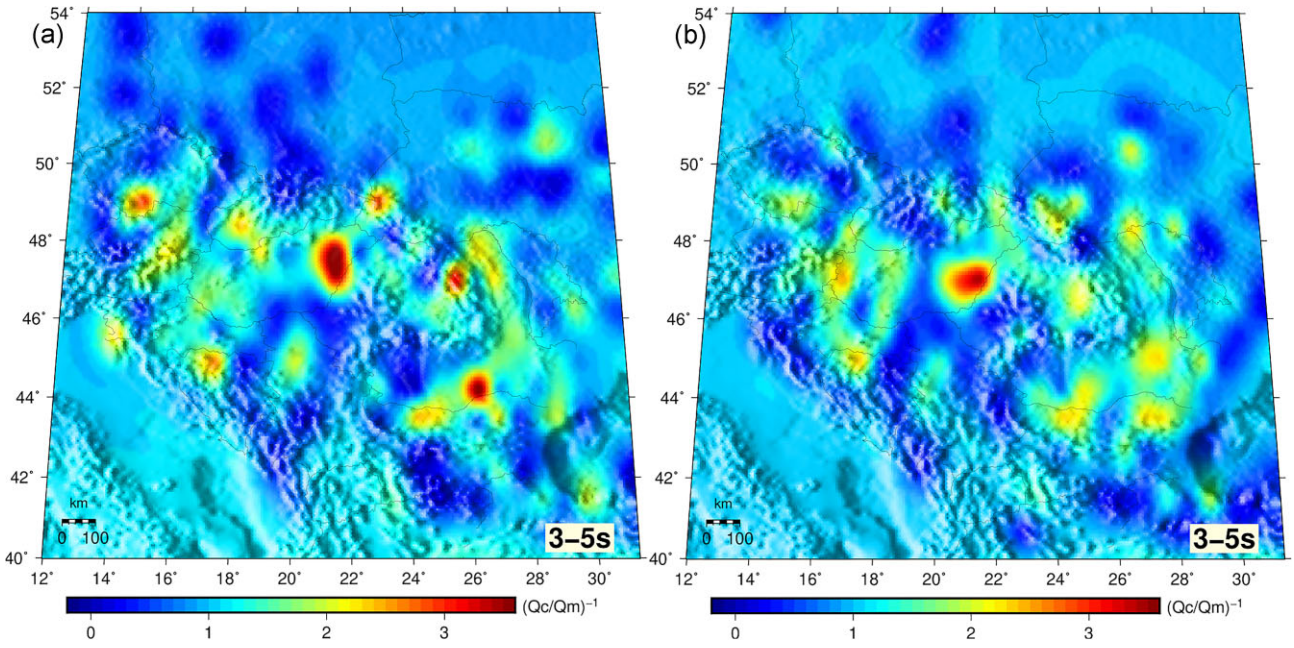

Figure 7. $(Qc/Qm)^{-1}$ maps for 3.0–5.0 period range computed for: (a) causal and (b) acausal signals. Red colours denote areas of high absorption while dark blue displays no absorption.

444 at 3–5 s, 401 for 5–10 s, 384 for 10–20 s and 333 for 20–30 s (Fig. S4, Supporting Information). Compared to average values estimated by Soergel *et al.* (2020) in the common period ranges, our average Qc values in the long-period domain (10–20 s) are roughly 16 per cent higher, while for shorter periods (5–10 s) we obtained an average Qc of about 15 per cent higher. Qc values do not exhibit dependence on calculated traveltimes for the selected period ranges (Fig. S4, Supporting Information), implying that our results are stable and reliable for the selected data set.

Our results show various attenuation heterogeneities across the CPR (Fig. 8). The highest attenuation (absorption) anomaly ($(Qc/Qm)^{-1} > 3$) appears in the northeast Pannonian region at low-period intervals (3–5 and 5–10 s, Fig. 8) and is strongly reduced in amplitude at longer periods (10–20 and 20–30 s). Similar $(Qc/Qm)^{-1}$ values appear in the Bohemian Massif, the East Carpathians and the Moesian Platform at low periods (3–5 s), but seem to disappear at long-period intervals. Intermediate-attenuation regions ($(Qc/Qm)^{-1} \sim 2$) include the transition between the Eastern Alps and the Western Carpathians, the Pannonian region north of the Mid-Hungarian Line (MHL) at low periods, the contact between the PB and the Dinarides (most evident at periods > 5 s), the TB (at all periods) and the South-East Carpathians. In contrast, low attenuation regions ($(Qc/Qm)^{-1} < 1$) are consistent at all periods in the central Pannonian region south of the MHL, the southern Apuseni Mountains and the western South Carpathians.

The maps showing the Qc distribution computed for each station in the selected period ranges are shown in Fig. 9. The average Qc values estimated per station (based on the ray coverage displayed in Fig. 5b) match well with the features emphasized by tomographic maps and geological units. However, the average Qc estimates per station show more variance in the 3–5 s period interval than those obtained for the longer period ranges (20–30 s). Qc results from the tomography model are based on a data set that has stricter quality control filters, as was previously mentioned, which could justify the observed differences.

6 DISCUSSION

The Eastern Europe region and adjacent areas were affected by significant tectonic deformation at different time periods, as shown above. In the subsequent sections, we discuss the results in relation to previous research and how well they match with the geology and geophysical properties of the region. Because we are assuming a diffusive medium, it must be considered that the attenuation structures revealed by the proposed approach are driven by the absorption process (see Section 4.3).

6.1 Comparison with results from previous seismic attenuation and velocity tomography

In contrast to previous attenuation studies of the Eastern European area (Herak 1991; Oancea *et al.* 1991; Kiszely 2000; Dasović *et al.* 2013; Gaebler *et al.* 2015; Borleanu *et al.* 2023), we employed ambient noise cross-correlations between various station pairs. By constructing virtual sources, this approach significantly enhances the quantity of data used, allowing us to image crustal attenuation features at the highest possible resolution. The selected period ranges, which are specific to these types of data, offer additional information that cannot be revealed through earthquake data analysis. A similar approach was recently applied by Soergel *et al.* (2020), which showed a consistent geographic pattern of high and low coda-Q over the broader Alpine area.

Common characteristics with the model of Soergel *et al.* (2020) are also shown by the attenuation maps (Fig. 8), which emphasize significant attenuation patterns in the upper and middle crust (3–5 and 5–10 s) of the Pannonian Basin (Fig. 8). Recent ambient noise tomography investigations (Ren *et al.* 2013; Szanyi *et al.* 2021) estimated low shear wave velocity in the upper crust under the Pannonian Basin, which correlates spatially with the strong attenuation patterns indicated by our attenuation tomography model. Although Soergel *et al.* (2020) argue that their study does not have

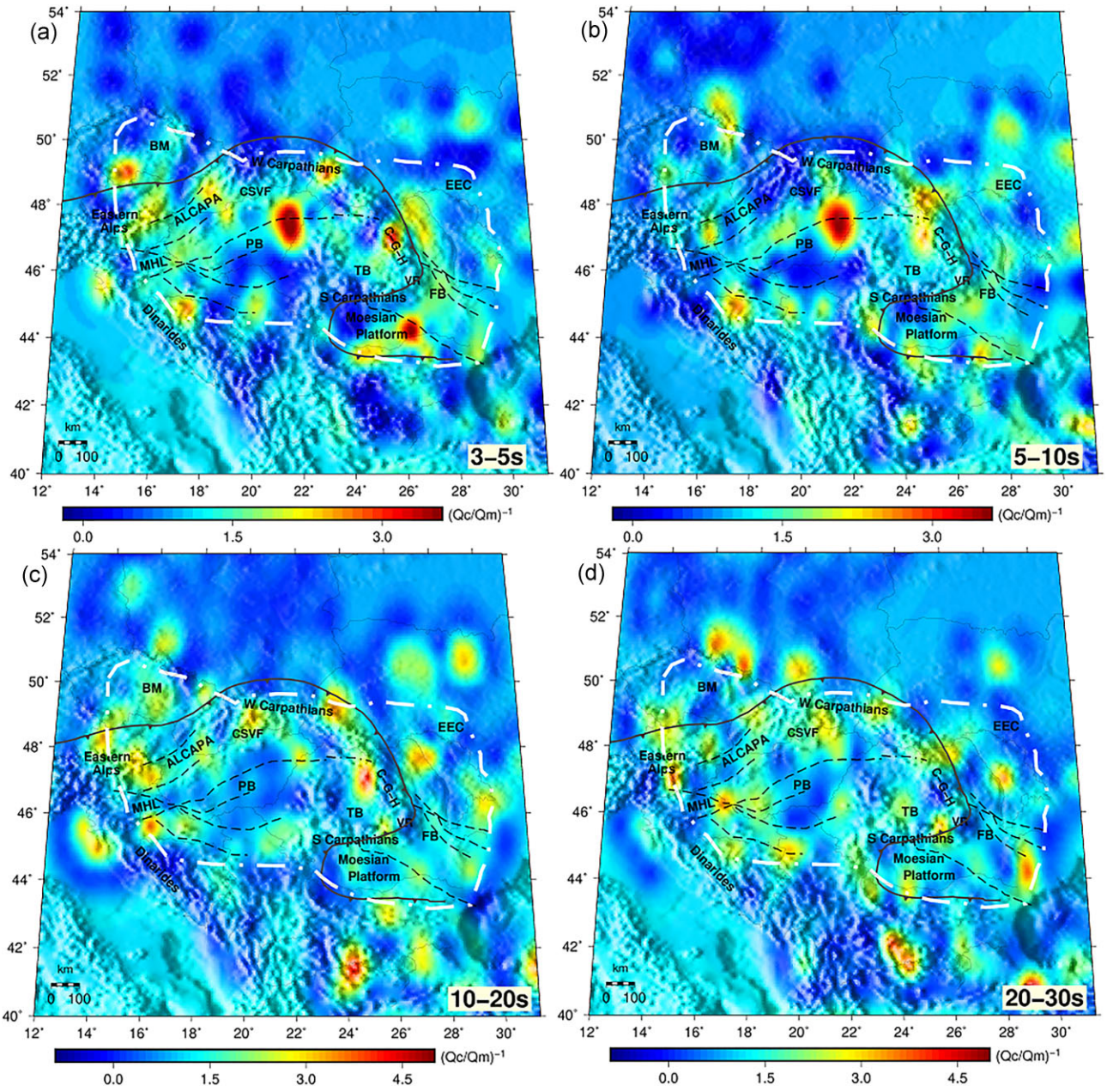

Figure 8. Attenuation maps expressed as $(Qc/Qm)^{-1}$ for selected period ranges: (a) 3.0–5.0 s, (b) 5.0–10.0 s, (c) 10.0–20.0 s and (d) 20.0–30.0 s. The red colour denotes areas of high absorption, and blue displays low absorption regions. Black dashed lines indicate major faults and tectonic boundaries. The white dashed line marks the area where our results have the highest resolution according to checkerboard tests. The abbreviations are as follows: BM: Bohemian Massif; C-G-H: Călimani–Gurghiu–Harghita volcanic chain; CSVF: Central Slovakia Volcanic Field; EEC: East European Craton; FB: Focşani Basin; PB: Pannonian Basin; MHL: Mid-Hungarian Line; TB: Transylvanian Basin and VR: Vrancea Region.

the highest ray's coverage for the Bohemian Massif area, where they obtained high attenuation, our results indicate similar attenuation patterns. In contrast, shear wave velocities in the upper crust of the Bohemian Massif exhibit a considerable degree of variability depending on the data coverage and analysis techniques (Hrubcová *et al.* 2005; Ren *et al.* 2013).

In Romania, our results partially match those of Oancea *et al.* (1991), who indicated considerable attenuation in the Eastern Carpathian volcanic area and Pannonian Basin and no attenuation in the TB. In contrast to their findings, we highlight moderate attenuation across the TB with a weak period dependence (Fig. 8). More recent waveform modelling in the South-East Carpathians indicated high attenuation in the Focşani Basin (Ardeleanu *et al.* 2022), similar to our findings for short periods.

For the contact between the Adriatic Plate and the Dinarides, our results are robust, particularly on the northern side (Fig. 6 and Fig. S7, Supporting Information), where significant and period-dependent attenuation patterns are revealed (Figs 8–11a). Ren *et al.* (2013) highlighted group velocities of Rayleigh waves and shear wave velocities with low values across this area. This is consistent with both the low values of *Qc* (high attenuation) highlighted by our analysis for the period range (3–30 s) and the small values of *Qc* determined from earthquake processing (between 1.5 and 24 Hz) by Dasović *et al.* (2013).

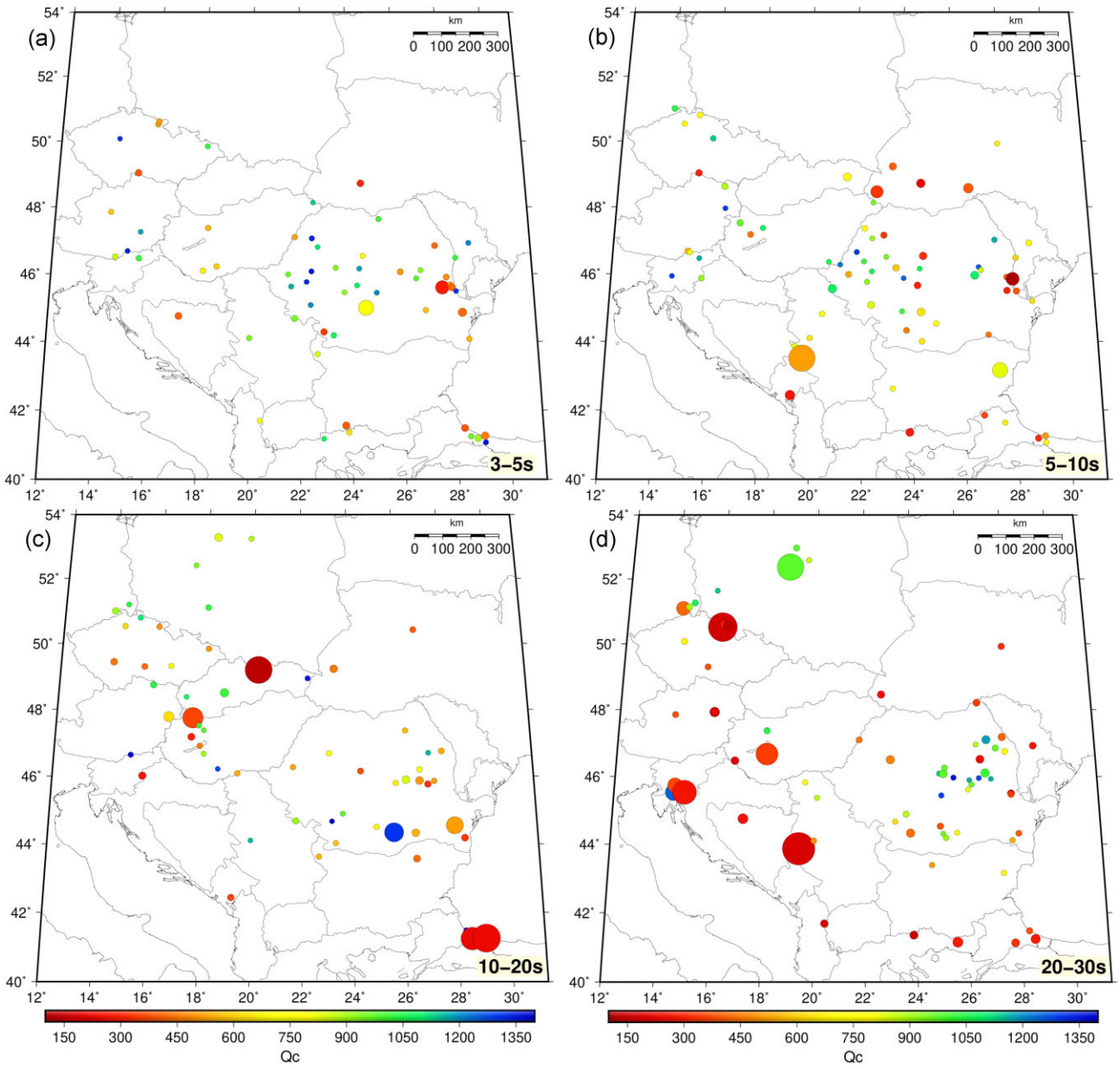

Figure 9. Maps showing the average *Qc* computed per station (coloured circles) in the following period ranges: (a) 3.0–5.0 s; (b) 5.0–10 s; (c) 10.0–20.0 s and (d) 20–30 s. The red colour indicates higher attenuation (lower *Qc* values) while blue suggests lower attenuation. The symbol size is inversely proportional to the standard deviation per station.

6.2 Attenuation of sedimentary basins

Fig. 10 shows the attenuation anomalies overlaid with Neogene sedimentary thickness contours. The map shows a clear correlation between most high-attenuation regions and sedimentary basins within the Carpathian-Pannonian system. The Southern and Eastern Carpathian foreland sedimentary basins show high attenuation patterns at short periods following the sinuous track of the Carpathian bend, but the model resolution decreases in the Western Carpathian foreland basin. The strongest attenuation regions do not directly correlate with the thickness of the Neogene strata. The Focșani Basin, the deepest forearc sedimentary basin (Bocin *et al.* 2013), has a high-absorption signature in the short-period range (3–10 s).

In the Moesian Platform, high attenuation patterns appear in its western section at low periods (3–5 s). Likely, the older Palaeozoic sediments deposited on top of the Moesian Platform from previous collisions and the heterogeneous basement topography (Seghedi *et al.* 2005) influence our measurements. Attenuation decreases with increasing period range, showing a good fit with previous studies that highlighted the presence of a Silurian sediment layer up to 1.2 km deep (Paraschiv 1979; Seghedi *et al.* 2005).

Seismic attenuation in the TB is moderate and weakly dependent on the period (Figs 8–10). The uplift tendencies, volcanic activity on its eastern edge (Seghedi *et al.* 2019) and active fault systems on its northern side (e.g. the Bogdan Vodă fault, Figs 1 and 11a) are all essential factors in seismic wave attenuation beneath this region.

The Pannonian Basin appears more heterogeneous in our 3–5 s attenuation map, but low *Qc* regions still partially correlate with known sedimentary basins, such as the Danube and Vienna Basins

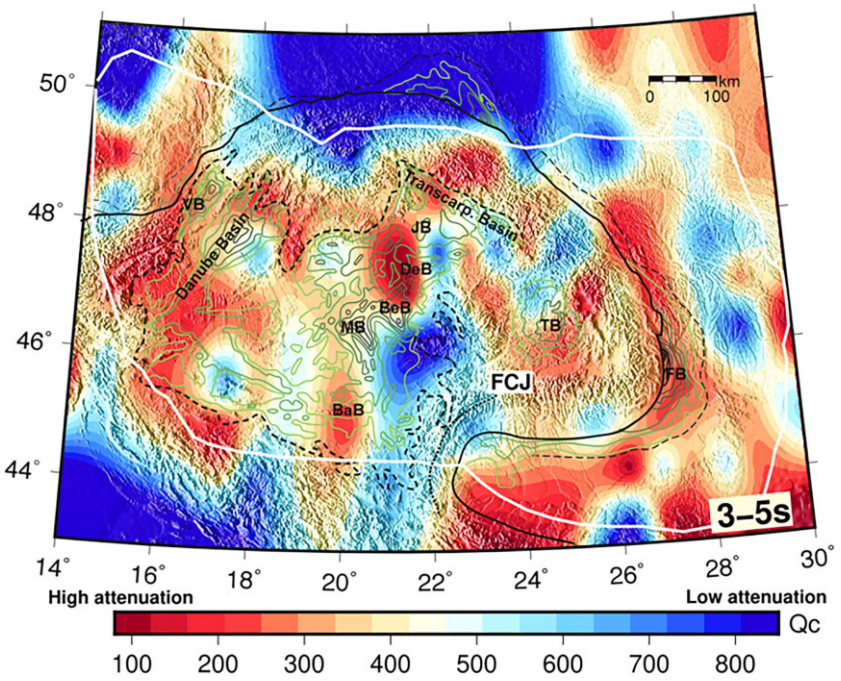

Figure 10. Attenuation (*Qc*) map in the 3–5 s period interval of the CPR, showing the thickness of Neogene sedimentary basins (green contours, after Kováč *et al.* 2007). Black dashed lines outline the Carpathian Foreland Basin and the Pannonian Basin. The thick black line marks the Alpine-Carpathian deformation front. The dotted black line shows the Cerna-Jiu Fault (FCJ). The white dashed line marks the area where our results have the highest resolution according to checkerboard tests. Abbreviations are as follows: VB: Vienna Basin, BaB: Backa Basin, MB: Mako Basin, BeB: Békés Basin, DeB: Derecske Basin, JB: Jászag Basin, TB: Transylvanian Basin and FB: Focşani Basin.

in the northwest and the Mako, Bekes, and Derecske Basins in the eastern Pannonian (Fig. 10), where the pre-Neogene basement depth reaches 7–8 km (Horvath *et al.* 2015). The Pannonian Basin has considerable attenuation in the short-period range (3–10 s), with a decreasing tendency in the long-period range. High attenuation structures are more prevalent in the northern Pannonian Basin than in the area south of the MHL. This confirms the results of Csontos & Nagymarosy (1998), who defined the MHL as a prominent tectonic feature of the Intra-Carpathian region that divides two terranes of different origin and tectonic structures.

6.3 Attenuation features of volcanic fields

Previous studies suggest that basalts can strongly attenuate and scatter seismic energy (e.g. Maresh *et al.* 2006). However, Eberhart-Phillips (2016) estimated high *Q* (low attenuation) in the Great Valley ophiolites. Here, we note a prominent high *Qc* in the Western Apuseni Mountains centred approximately around 22°E, 46°N (Fig. 10). Here, the Vardar Ophiolites, buried beneath Transylvania, outcrop in an elongated E-W band in the Apuseni Mountains and extend to the west beneath the Neogene sediments of the Pannonian Basin. The CGH Volcanic Belt in the Eastern Carpathians and the CSVF in the Western Carpathians (Fig. 1a), the largest exposed intermediate calc-alkaline volcanic fields in the Carpathian-Pannonian System, appear as medium-to-high attenuation areas (Figs 8 and 11a). The CGH Volcanic Belt in the Eastern Carpathians shows significant attenuation, especially at short periods (3–5 and 5–10 s), in contrast with the CSVF area, which is better highlighted in longer period ranges (10–20 and 20–30 s). One potential explanation for this variability can be attributed to age and structural variations. The CSVF area consists of calc-alkaline volcanic rocks (16.5–2 Ma), whereas the CGH region is characterized by potassic-ultrapotassic Quaternary volcanism (< 2 Ma; Harangi 2001). Low *Vp* and *Vs* in the crust beneath the two volcanic areas were also revealed by recent ambient noise tomography studies (Ren *et al.* 2013).

6.4 Possible relationships between attenuation and seismic activity

Previous research (Mitchell 1995; Fillipuci et al. 2021) suggested that seismic activity may correlate with attenuation: low attenuation (high *Qc*) regions are characterized by poor seismicity, whereas areas with intense seismic activity have high attenuation (low $Qc < 200$). To further analyse the presumed connection between seismic activity and attenuation features, we displayed in Fig. 11(a) the tomographic image obtained for *Qc* (in 5–10 s) on which we superimposed the main fault systems, volcanic units, and seismic events ($M > 3$) recorded in the study region between 2013 August and 2023 February, according to the European Mediterranean Seismological Centre (EMSC). Romania is characterized by considerable seismic activity at the crustal level at the bending of the Eastern Carpathians (Vrancea, Focşani Basin), where our results indicate low *Qc* (<200) and the attention maps reveal notable attenuation features (Figs 8 and 11a). Significant seismic activity was recorded in the Southern Carpathians (Radulian *et al.* 2000; Popa *et al.* 2022), an area associated with substantial attenuation (small *Qc*) in the eastern section, cross-cut by a north–south oriented band of high *Qc* (>400). Fig. 11(a) shows that all epicentres in this area overlap the moderate and high attenuation features. The Banat area (BA-western Romania), which is also one of the seismically active areas, is characterized by moderate to low attenuation at short periods with an increasing trend toward longer

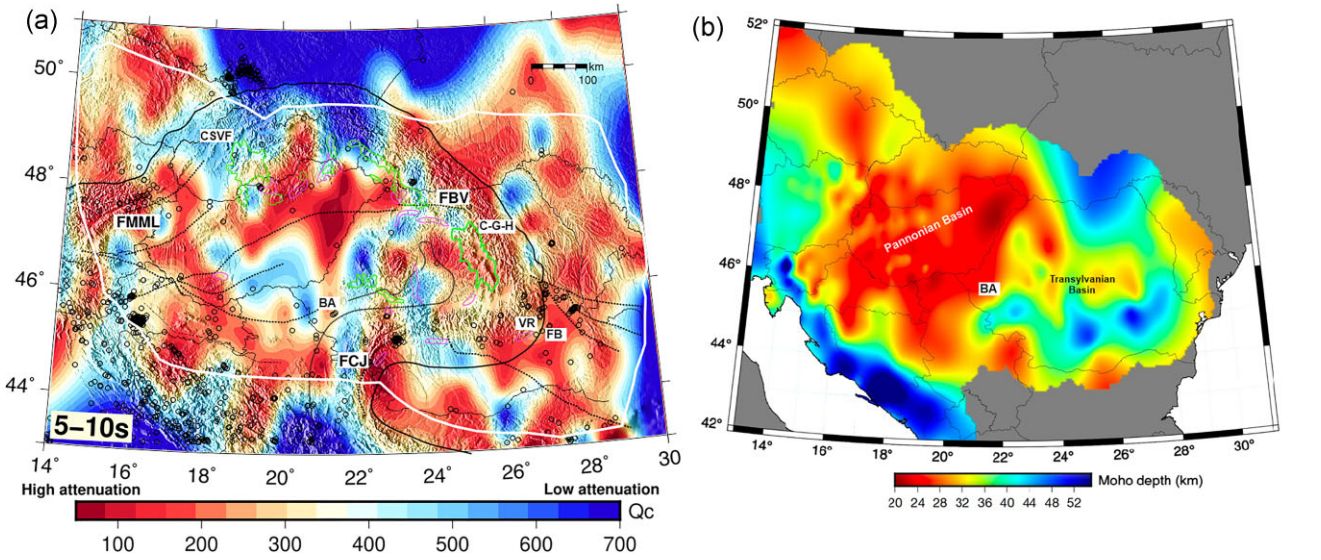

Figure 11. (a) Attenuation (Qc) map in the 5–10 s period range, of the CPR, showing the main fault systems and tectonic boundaries (dashed black lines), and $M > 3$ crustal seismicity (circles) with hypocentral depths, $H < 50$ km, recorded between 2010 and 2023, according to EMSC. The thick black line marks the Alpine-Carpathian deformation front. Green lines mark the intermediate-grade volcanic outcrops. Magenta lines are felsic volcanic outcrops. The white dashed line marks the area where our results have the highest resolution according to checkerboard tests. (b) The Moho depth variation in Eastern Europe and neighbouring areas, determined using the most recent receiver function investigations undertaken in these regions (Petrescu *et al.* 2019; Stipčević *et al.* 2020; Kálmar *et al.* 2021; Mroczek *et al.* 2023). Abbreviations are as follows: FBV: Bogdan Vodă Fault; FCJ: Cerna-Jiu Fault; FMML: Mur-Murz Fault; BA: Banat region; VR: Vrancea region and FB: Focșani Basin.

periods. Here, earthquake epicentres overlap regions dominated by at least moderate attenuation features or transition areas from low to strong attenuation regimes, possibly pointing to different earthquake generation mechanisms than those acting in high-attenuation areas.

A distinct attenuation signature may be observed at the bending of the Southern Carpathians. Romania has recently experienced an unprecedented crustal seismic sequence in this area (starting on 2023 February 13), with two major shocks (2023 February 13; $M_L = 5.2$ and 2023 February 14; $M_L = 5.7$) and a thousand aftershocks (reported until 2023 March 1) distributed near the upper segment of the Tertiary age Cerna-Jiu Fault (FCJ, Fig. 11a). This fault, which stretches between the Southern Carpathians and the Moesian Platform, is mainly known for the earthquakes on its lower segment, revealing a large variety of earthquake-generating mechanisms (Popa *et al.* 2018; Radulian *et al.* 2020; Oros *et al.* 2021). Our model shows period-dependent attenuation, in line with previous studies that highlighted comparable characteristics for regions with substantial tectonic heterogeneities (Kiszely 2000; Borleanu *et al.* 2017). The lower section of the FCJ exhibits high attenuation characteristics across a wide period range (3–5 and 5–10 s, Figs 8, 10 and 11a). Still, the upper segment exhibits strong attenuation properties only in the shortest period range (3–5 s). This attenuation variability might imply differing depths of the fault system associated with the major fault (FCJ), heterogeneous fluid distribution along the fault, or a change in rock composition for the upper segment compared to the lower one (Oros *et al.* 2021). Our results indicate that for short periods (3–5 s), there is a lower attenuation along the FCJ (Fig 10), whereas, for longer periods (5–10 s), the attenuation is more prominent (Fig 11a). This transition from less pronounced attenuation in the uppermost crust to stronger attenuation at higher depths can be explained by several factors, including variations in lithology, mineralogy, or temperature, stress changes, or the presence of anisotropy or fluids (De Siena *et al.* 2014; Borleanu *et al.* 2017; Napolitano *et al.* 2020; Gabrielli *et al.* 2022). Previous research in this area (Demetrescu & Andreescu 1994; Ioane & Ion 2005) showed a low heat flow tendency and negative Bouguer anomalies, indicating a cold and less dense environment. In this context, the seismic activity generated on distinct segments of the FCJ may be influenced by fluid migration (Popa *et al.* 2018; Borleanu *et al.* 2023) or, even more, a fluid-saturated medium, which explains how attenuation operates in this realm. The presence of fluids may be favoured by the extensional tectonic regime that characterizes the area and is assumed to be an important factor in explaining the unusual duration of the aftershock activity recorded after the two main shocks of 2023 February (aftershock activity is still ongoing at present, 2023 August).

Seismic activity in Hungary is relatively modest, with intensification found particularly along the edges of the Pannonian Basin, especially in mountainous areas, at the contact with the Dinarides and the Eastern Alps. In these regions, our results show moderate attenuation in the long-period band (10–30 s), increasing in the short period (5–10 s). A notable attenuation anomaly independent of the period range emerges around the Mur-Murz Fault (FMML), which hosts intense seismic activity (Figs 8, 9 and 11a). In the short-period range (3–10 s), our maps indicate significant attenuation features in the central and northeastern sectors of the Pannonian Basin, where seismic activity is scarce, highlighting low Qc values associated with less deformable areas. In this area, high attenuation correlates with low seismic wave velocities as well, likely due to the presence of hydrothermal fluids (Wéber 2002), which may play a role in earthquake nucleation (e.g. Zhao *et al.* 1996). The contact zone between the Dinarides and the Adriatic microplate is seismically active and also shows substantial attenuation in the short-period band (Fig. 11a), supporting the global correlation between active seismic areas and low Qc (Filippucci *et al.* 2021).

6.5 Potential links between attenuation and crustal thickness

The inversion technique normalizes the energy density over the entire inversion grid, implying that there is no energy leakage along its deep and lateral edges (De Siena *et al.* 2017). While applying sensitivity kernels, it has been demonstrated that this approximation works for the lateral edges (Sketsiou *et al.* 2020). Radiative transfer simulations across oceanic basins show that shallow Moho depths produce low coda decays even at later lapse times (Nardoni *et al.* 2021), resulting in anomalous attenuation patterns where Moho depths might control the full seismic wavefield (Nardoni *et al.* 2023). It is thus essential to compare the results of the *Qc* inversion with those of receiver functions. To determine how the variation of the crust thickness may impact coda quality factors of Rayleigh waves, we mapped in Fig. 11(b) an interpolated model of Moho depth based on the values available in the latest receiver function studies carried out in this area (Petrescu *et al.* 2019; Stipčević *et al.* 2020; Kálmar *et al.* 2021; Mroczek *et al.* 2023).

The Pannonian Basin is characterized by a thin crust (∼28 km), on its entire surface (Fig. 11b). Our attenuation plots highlight significant attenuation features, especially in the short-period ranges, distributed mostly toward the northeast, at the contact with the Western Carpathians (Figs 8, 10 and 11), where the recent tomography studies indicate predominantly low seismic velocities (Weber 2002; Ren *et al.* 2013). The TB is also characterized by a relatively thin crust (∼32 km, Fig. 11b) correlated with moderate attenuation features and low velocities, especially in the upper crust (Borleanu *et al.* 2021). These two examples clearly demonstrate that changes in Moho depth do not have a significant impact on the coda-attenuation of Rayleigh waves. On the one hand, this specific pattern may be explained by the period range used in our study (3–30 s) as compared with the period range (0.66–2 s) used by Nardoni *et al.* (2021) in their simulations, or it could be detected only in the oceanic settings, where the Moho is significantly shallower (∼15 km). The attenuation patterns highlighted in the Pannonian basin and TB rather match the findings of Shapiro *et al.* (1996) and Baumgardt (2001) who linked the attenuation of crustal phases with the accumulation of sediments in various sedimentary basins, the energy being transferred into slow shear waves captured within different sedimentary layers. At the same time, areas with thicker crust (e.g. the Dinarides or the Moesian Platform, Figs 8, 10 and 11) overlap with areas with significant attenuation that barely depend on the period range. Although the sedimentary layer in these areas is thin, high attenuation may be caused by the strong tectonic heterogeneity, complex fault systems, and the presence of fluids.

7 CONCLUSIONS

By analysing the broad-band vertical recordings from the stations that were operational in 1999, 2005–2007, 2009–2011 and 2020 in Eastern Europe, we computed cross-correlations between various station pairs to extract waves propagating between the stations. The *Qc* values have been determined using two strategies: direct measurements of the decay of the envelope of the coda of the Rayleigh waves and their inversion using the MuRAT2D algorithm and the sensitivity kernels. Both methods indicate that *Qc* in Eastern Europe and surrounding areas is decreasing with the period, as has been previously emphasized. Although the results obtained by both methods highlight appropriate attenuation characteristics, the tomographic maps obtained from the inversion have a higher degree of reliability, as seen by the results of the synthetic tests. Also, the correlation with geology is sharper for the tomography attenuation images than on maps, where the average *Qc* determined per station is emphasized.

Strong attenuation anomaly patches appear in the northeast Pannonian region, the Bohemian Massif, the East Carpathians and the Moesian Platform, in lower frequency intervals, suggesting the presence of heterogeneous structures within upper crustal sedimentary layers, possibly caused by locally fluid-lubricated faults, high-temperature anomalies, or high water-content mineralogy. Volcanic structures exhibit distinct attenuation properties, with a significant period dependence, reflecting their age differences and different rock compositions.

Our analysis reveals a considerable correlation between low *Qc* values and areas with intense seismic activity, as well as a substantial dependency of *Qc* on period in areas with strong tectonic heterogeneity. At the same time, we identified particular places where the correlation between seismic activity and attenuation is negative. Besides that, our results demonstrate that there is no association between areas with low attenuation and regions with a shallower Moho.

Attenuation maps have a direct impact on seismic hazard; hence, it is important to quantify the contribution of seismic attenuation studies in seismic hazard research in order to improve the identification of regions that are vulnerable to strong earthquakes. Our results show weak attenuation areas in the southwest, southeast and northeast of the Eastern Carpathian bending, which correspond to the areas that were most exposed to the damages caused by previous major earthquakes ($M > 7$) that occurred in Vrancea.

SUPPORTING INFORMATION

Supplementary data are available at *GJI* online.

Figure S1. (a) Example of estimated Rayleigh wave Green's functions (acausal and causal sections) in, (a) 5–10 s and (b) 10–20 s, for paths between VOIR and the stations, placed up 500 km away.
Figure S2. Examples of cross-correlograms (top) computed between different pairs of stations (in Romania, Fig. 3d) and their envelopes (bottom), indicating decay of the coda waves in time, bandpass filtered in the following period ranges: (a) 3–5 s; (b) 5–10 s; (c) 10–20 s and (d) 20–30 s. Vertical black lines delimit the coda window and lapse time, while the dashed black line displays the slope for envelope decay. The station pairs are shown in the upper right corner of the bottom plot of Fig. S2d).
Figure S3. *Qc* in 5–10 s period range as a function of backazimuth at distances of 50–250, 250–500 and 500–1000 km.
Figure S4. Inverse *Qc* dependence on traveltime for (a) 3–5 s, (b) 5–10 s, (c) 10–20 s and (d) 20–30 s.
Figure S5. Number of correlations as a function of: (a) interstation distance and (b) backazimuth.
Figure S6. *Qc* sensitivity computed for 5–10 s period range between a source (station PA82 of 7E network) and a receiver (station PF47 of 7E network)
Figure S7. The final ray path coverage as resulted from the inversion algorithm in each of the period ranges: (a) 3–5 s, (b) 5–10 s, (c)10–20 s and (d) 20–30 s.

Oxford University Press is not responsible for the content or functionality of any supporting materials supplied by the authors. Any queries (other than missing material) should be directed to the corresponding author for the paper.

ACKNOWLEDGMENTS

The present study was partially funded by the EENSANE (East European Ambient Seismic Noise, Project PN-III-P4-ID-PCE-2020–2972); AFROS (Analysis and Forecasting of Romanian Seismicity, Project PN-III-P4-ID-PCE-2020–1361); PhENOMeNAL (Virtual Platform for the Collection and Interactive Analysis of Multidisciplinary Geophysical Data, Project PN-IIIP2- 2.1-PED-2019–1693); DISSA (Data-intensive study of intermediate-depth and shallow seismic activity in Romania: from regular earthquakes to tectonic tremor, Project PN-III-P1-1.1-TE2019-1797), all supported by UEFISCDI (Executive Agency for Higher Education, Research, Development and Innovation Funding), Romania; the PNRR-DTEClimate nr. 760008/31.12.2023, the Nucleu Program SOL4RISC, projects nos PN23360101 and PN23360201, supported by the Romania Ministry of Research, Innovation and Digitalization; Integrated thematic services in the field of Earth observation: a national platform for innovation (SETTING) co-funded from the European Regional Development Fund (FEDR) through the Operational Competitivity Programme 2014–2020 (contract no. 336/390012). The authors also acknowledge the Mobility project (PN-III-P1-1.1-MC-2019–2118) funded by UEFISCDI and the HPC17VM07K grant awarded by the HPC-Europa3 Transnational Access program, which supported two research visits (in 2019 and 2022) of the first author at the Institute of Geoscience, Johannes Gutenberg University, Germany, as well as access to the German HPC Center (HLRS). HPC-Europa3 is supported by the European Commission H2020 Research and Innovation GA no. 730897. FM has received funding from the Deutsche Forschungsgemeinschaft (DFG—German Research Foundation) under the Individual Research Project: SI 1748/4–1. Most figures were made using GMT software (Wessel *et al.* 2013). The authors are also grateful to the two anonymous reviewers who read the manuscript carefully and provided critical and helpful feedback. FB, LP and AOP processed and visualized the noise data. FB and LP wrote the original draft. LDS provided supervision and conceptualized the MuRAT algorithm. FM, BG, MR and LDS reviewed and edited the manuscript. All authors have read, agreed and participated in the submitted version of the manuscript.

DATA AVAILABILITY

Data analysed in this study were obtained from the National Institute for Earth Physics (NIEP), through the Romanian Seismic Network (https://doi.org/10.7914/SN/RO), the Main Centre for Special Monitoring of Ukraine (https://doi.org/10.7914/SN/UD), the EIDA; Observatories & Research Facilities for European Seismology (ORFEUS-http://www.orfeus-eu.org/) and Incorporated Research Institutions for Seismology (IRIS-http://ds.iris.edu/ds/nodes/dmc/).

DECLARATION OF COMPETING INTERESTS

The authors declare that they do not have any known competing financial interests or relationships that could appear to have influenced the work disclosed in this study.

REFERENCES

Aki, K., 1980. Attenuation of shear waves in the lithosphere for frequencies from 0.05 to 25 hz, *Phys. Earth planet. Inter.,* **21,** 50–60.

Aki, K. & Chouet, B., 1975. Origin of coda waves: source, attenuation, and scattering effects, *J. geophys. Res.,* **80,** 3322–3342.

Allmark, C., Curtis, A., Galetti, E. & de Ridder, S., 2018. Seismic attenuation from ambient noise across the North Sea Ekofisk permanent array, *J. geophys. Res. Solid Earth,* **123,** 8691–8710.

Ardeleanu, L., Neagoe, C., Placintă, A.O. & Coman, A., 2022. On the seismic wave attenuation at the bend of the Southeastern Carpathians, *J. Seismol*., **27,** 233–240.

Bada, G., 1999. *Cenozoic Stress Field Evolution in the Pannonian Basin and Surrounding Orogens, Inferences from Kinematic Indicators and Finite Element Modeling,* PhD thesis, Vrije University, Amsterdam, Netherlands.

Baumgardt, D., 2001. Sedimentary basins and the blockage of lg wave propagation in the continents. *Pure appl. Geophys.,* **158,** 1207–1250.

Bektaş, Ö., 2013. Thermal structure of the crust in Inner East Anatolia from aeromagnetic and gravity data, *Phys. Earth Planet.,* **221,** 27–37.

Bensen, G.D., Ritzwoller, M.H., Barmin, M.P., Levshin, A.L., Lin, F., Moschetti, M.P., Shapiro, N.M. & Yang, Y., 2007. Processing seismic ambient noise data to obtain reliable broad-band surface wave dispersion measurements, *Geophys. J. Int.,* **169,** 1239–1260.

Bocin, A., Stephenson, R., Mațenco, L. & Mocanu, V., 2013. Gravity and magnetic modeling in the Vrancea Zone, south-eastern Carpathians: redefinition of the edge of the East European Craton beneath the south-eastern Carpathians, *J. Geodyn.,***71,** 52–64.

Borleanu, F., De Siena, L., Thomas, C., Popa, M. & Radulian, M., 2017. Seismic scattering and absorption mapping from intermediate-depth earthquakes reveals complex tectonic interactions acting in the Vrancea region and surroundings (Romania), *Tectonophysics*., **706,** 129–142.

Borleanu, F., Petrescu, L., Enescu, B., Popa, M. & Radulian, M., 2021. The missing craton edge: crustal structure of the East European Craton beneath the carpathian Orogen revealed by double-difference tomography, *Global Planet. Change,* **197,** 103390. doi: 10.1016/j.gloplacha.2020.103390.

Borleanu, F., Petrescu, L., Seghedi, I., Thomas, C. & De Siena, L., 2023. The seismic attenuation signature of collisional orogens and sedimentary basins within the Carpathian Orogen, *Global Planet. Change,* **223,** 104093. doi: 10.1016/j.gloplacha.2023.104093.

Calvet, M. & Margerin, L., 2013. Lapse-time dependence of coda Q: anisotropic multiple-scattering models and application to the Pyrenees, *Bull. seism. Soc. Am.,* **103**(3), 1993–2010.

Calvet, M., Sylvander, M., Margerin, L. & Villaseñor, A., 2013. Spatial variations of seismic attenuation and heterogeneity in the Pyrenees: coda Q and peak delay time analysis, *Tectonophysics,* **608,** 428–439.

Ciulavu, D., 1999. *Tertiary Tectonics of the Transylvanian Basin,* PhD thesis, Vrije Univ., Amsterdam, Netherlands.

Ciulavu, D., Dinu, C., Szakacs, A. & Dordea, D., 2000. Neogene kinematics of the Transylvanian Basin, Romania, *AAPG Bull.,* **84**(10), 1589–1615.

Constantin, A.P., Moldovan, I.A., Partheniu, R., Grecu, B. & Ionescu, C., 2021. Relation between macroseismic intensity and peak ground acceleration and velocity for the Vrancea (Romania) subcrustal earthquakes, *Ann. Geophys.,* **64,** SE432. doi: 10.4401/ag-8448.

Csontos, L. & Nagymarosy, A., 1998. The Mid-Hungarian line: a zone of repeated tectonic inversions, *Tectonophysics,* **297,** 51–71.

Csontos, L., Nagymarosy, A., Horváth, F. & Kovác, M., 1992. Cenozoic evolution of the intra-carpathian area: a model, *Tectonophysics,* **208,** 221–241.

Dando, B.D.E., Stuart, G.W., Houseman, G.A., Hegedüs, E., Brückl, E. & Radovanović, S., 2011. Teleseismic tomography of the mantle in the carpathian-pannonian region of central Europe, *Geophys. J. Int.,* **186,** 11–31.

Dasović, I., Herak, M. & Herak, D., 2013. Coda-Q and its lapse time dependence analysis in the interaction zone of the Dinarides, the Alps and the Pannonian basin, *Phys. Chem. Earth,* **63,** 47–54.

De Siena, L., Amoruso, A., Del Pezzo, E., Wakeford, Z., Castellano, M. & Crescentini, L., 2017. Space-weighted seismic attenuation mapping of the aseismic source of Campi Flegrei 1983–1984 unrest, *Geophys. Res. Lett.,* **44,** 1740–1748.

De Siena, L., Thomas, C., Waite, G.P., Moran, S.C. & Klemme, S., 2014. Attenuation and scattering tomography of the deep plumbing system of Mount St. Helens, *J. geophys. Res. Solid Earth,* **119,** 8223–8238.

Del Pezzo, E., Ibañez, J., Prudencio, J., Bianco, F. & De Siena, L., 2016. Absorption and scattering 2-d volcano images from numerically calculated space-weighting functions, *Geophys. J. Int.,* **206,** 742–756.

Demetrescu, C. & Andreescu, M., 1994. On the thermal regime of some tectonic units in a continental collision environment in Romania, *Tectonophysics,* **230,** 265–276.

Demetrescu, C., Nielsen, S.B., Ene, M., Şerban, D.Z., Polonic, G., Andreescu, M., Pop, A. & Balling, N., 2001. Lithosphere thermal structure and evolution of the Transylvanian Depression – insight from new geothermal measurements and modelling results, *Phys. Earth planet.,* **126**(3–4), 249–267.

Di Martino, M.D.P., De Siena, L. & Tisato, N., 2022. Pore space topology controls ultrasonic waveforms in dry volcanic rocks, *Geophys. Res. Lett.,* **49,** e2022GL100310. doi: 10.1029/2022GL100310.

Eberhart-Phillips, D., 2016. Northern California seismic attenuation: 3-D qp and qs models, *Bull. seism. Soc. Am.,* **106,** 2558–2573.

Enescu, B., Ghita, C., Moldovan, I.-A. & Radulian, M., 2023. Revisiting Vrancea (Romania) intermediate-depth seismicity: some statistical characteristics and seismic quiescence testing, *Geosciences,* **13,** 219. doi: 10.3390/geosciences13070219.

European Mediterranean Seismological Centre (EMSC), https://www.emsc-csem.org/#2, accessed 2023 Mar 01.

Ferrand, T.P. & Manea, E.F., 2021. Dehydration-induced earthquakes identified in a subducted oceanic slab beneath Vrancea, Romania, *Sci. Rep.,* **11,** 10315. doi: 10.1038/s41598-021-89601-w.

Filippucci, M., Lucente, S., Del Pezzo, E., de Lorenzo, S., Prosser, G. & Tallarico, A., 2021. 3D-Kernel based imaging of an improved estimation of (Qc) in the Northern Apulia (Southern Italy). *Appl. Sci. 2021,* **11**(16), 7512. doi: 10.3390/app11167512.

Fodor, L., Csontos, L., Bada, G., Györfi, I. & Benkovics, L., 1999. Tertiary tectonic evolution of the Pannonian Basin system and neighbouring orogens: a new synthesis of paleostress data, in *The Mediterranean Basins: Tertiary Extension within the Alpine Orogen,* pp. 295–334, eds: Durand, B., Jolivet, L., Horváth, F. & Séranne, M., Geological Society of Special Publications, 156.

Frankel, A., McGarr, A., Bicknell, J., Mori, J., Seeber, L. & Cranswick, E., 1990. Attenuation of high-frequency shear waves in the crust: measurements from New York State, South Africa, and southern California, *J. geophys. Res.,* **95,** 17,441–417,457.

Gabrielli, S., Akinci, A., Ventura, G., Napolitano, F., Del Pezzo, E. & de Siena, L., 2022. Fast-changes in seismic attenuation of the upper crust due to fracturing and fluid migration: the 2016-2017 Central Italy seismic sequence, *Front. Earth Sci. Sect. Struct. Geol. Tect.,* **10,** 1–18.

Gaebler, P.J., Sens-Schönfelder, C. & Korn, M., 2015. The influence of crustal scattering on translational and rotational motions in regional and teleseismic coda waves, *Geophys J. Int.,* **201,** 355–371, http://doi.org/10.1093/gji/ggv006.

Gee, D.G. & Stephenson, R.A., 2006. The European lithosphere: an introduction, in: *European Lithophere Dynamics,* eds: Gee, D. G. & Stephenson, R. A., Geological Society of London Memoirs, Vol. **32,** pp. 1–9.

Grecu, B., Neagoe, C. & Tataru, D., 2012. Seismic noise characteristics at the Romanian broadband Seismic network, *J. Earthq. Eng.,* **16,** 644–661.

Hansen, P.C. & O'Leary, D.P., 1993. The use of the L-curve in the regularization of discrete ill-posed problems, *SIAM J. Sci. Comput.,* **14,** 1487–1503.

Harangi, S., 2001. Neogene to quaternary volcanism of the Carpathian–Pannonian Region—a review, *Acta Geol. Hung.,* **44,** 223–258.

Havskov, J., Sørensen, M.B., Vales, D., Özyazıcıoğlu, M., Sánchez, G. & Li, B., 2016. Coda Q in different tectonic areas, influence of processing parameters, *Bull. seism. Soc. Am.,* **106,** 956–970.

Hennino, R., Trégourès, N., Shapiro, N.M., Margerin, L., Campillo, M., van Tiggelen, B.A. & Weaver, R.L., 2001. Observation of equipartition of seismic waves, *Phys. Rev. Lett.,* **86,** 3447–3345.

Herak, M., 1991. Lapse time dependent qc-spectra observed in the Dinarides region (Yugoslavia). *Phys. Earth planet.,* **67,** 303–312.

Horváth, F. *et al.* 2015. Evolution of the Pannonian basin and its geothermal resources, *Geothermics,* **53,** 328–352.

Horváth, F., Bada, G., Szafian, P., Tari, G., Adam, A. & Cloetingh, S.A.P.L., 2006. Formation and deformation of the Pannonian Basin: constraints from observational data, *European Lithosphere Dynamics,* eds: Gee, D. G. & Stephenson, R.A., Geological Society of London Memoirs, pp. 191–206, Vol., **32**.

Hrubcová, P., Środa, P., Špičák, A., Guterch, A., Grad, M., Keller, G.R., Brueckl, E. & Thybo, H., 2005. Crustal and uppermost mantle structure of the Bohemian Massif based on CELEBRATION 2000 data, *J. geophys. Res.,* **110,** B11305.

Huismans, R.S., Bertotti, G., Ciulavu, D., Sanders, C.A.E., Cloetingh, S. & Dinu, C., 1997. Structural evolution of the Transylvanian Basin (Romania), a sedimentary basin in the bend zone of the Carpathians, *Tectonophysics,* **272,** 249–268.

Ioane, D. & Ion, D., 2005. A 3D crustal gravity modelling of the Romanian territory, *J. Balkan Geophys. Soc.,* **8,** 189–198.

Ismail-Zadeh, A., Mațenco, L., Radulian, M., Cloetingh, S. & Panza, G., 2012. Geodynamics and intermediate-depth seismicity in Vrancea (the south-eastern Carpathians): current state-of-the-art, *Tectonophysics,* **530–531,** 50–79.

Kalmár, D., Hetényi, G., Balázs, A. & Bondár, I. AlpArray Working Group, 2021. Crustal thinning from orogen to Back-arc basin: the structure of the pannonian basin region revealed by P-to-S converted seismic waves, *J. geophys. Res.—Solid Earth,* **126**(7). doi: 10.1029/2020JB021309.

Kästle, E., Soomro, W.R., Boschi, L.C. & Meier, T., 2016. Two-receiver measurements of phase velocity: cross-validation of ambient-noise and earthquake-based observations, *Geophys. J. Int.,* **207**(3), 1493–1512.

King, T., De Siena, L., Benson, P. & Vinciguerra, S., 2023. Mapping faults in the laboratory with seismic scattering 1: the laboratory perspective, *Geophys. J. Int.,* **232**(3), 1590–1599.

Kiszely, M., 2000. Attenuation of coda waves in Hungary, *Acta Geod. Geophys. Hungarica,* **35,** 465–473.

Konečný, V. *et al.* 1995. Alkali basalt volcanism in Southern Slovakia: volcanic forms and time evolution, *Acta Vulcanol,* **7,** 167–172.

Kováč, M. *et al.* 2007. Badenian evolution of the Central Paratethys Sea: paleogeography, climate and eustatic sea-level changes, *Geol. Carpathica,* **58,** 579–606.

Krézsek, Cs. & Filipescu, S., 2005. Middle to late Miocene sequence stratigraphy of the Transylvanian Basin (Romania). *Tectonophysics,* **410**(1-4), 437–463.

Lorinczi, P. & Houseman, G., 2010. Geodynamical models of lithospheric deformation, rotation, and extension of the Pannonian Basin of Central Europe, *Tectonophysics,* **492**(1-4), 73–87.

Magrini, F., Boschi, L., Gualtieri, L., Lekić, V. & Cammarano, F., 2021. Rayleigh-wave attenuation across the conterminous United States in the microseism frequency band, *Sci. Rep.,* **11,** 10149.

Maresh, J., White, R.S., Hobbs, R.W. & Smallwood, J.R., 2006. Seismic attenuation of Atlantic margin basalts: observations and modeling, *Geophysics,* **71**(6), B211–B221.

Margerin, L., 2017. Breakdown of equipartition in diffuse fields caused by energy leakage, *Eur. Phys. J. Spec. Top.,* **226,** 1353–1370.

Martin, M. & Ritter, J.R.R. the CALIXTO working group, 2005. High-resolution teleseismic body-wave tomography beneath SE Romania—I. Implications for three-dimensional versus one-dimensional crustal correction strategies with a new crustal velocity model, *Geophys. J. Int.,* **162**(2), 448–460.

Mațenco, L., Balázs, A., Nader, F.A., Haq, B.U. & Fodor, L., 2022. Advances in the understanding of multiscale and coupled evolution of orogens, sedimentary basins and the underlying lithosphere, *Global Planet. Change,* **208,** 103689. doi: 10.1016/j.gloplacha.2021.103689.

Mațenco, L. & Radivojević, D., 2012. On the formation and evolution of the Pannonian basin: constraints derived from the structure of the junction area between the Carpathians and Dinarides, *Tectonics,* **31**(6). doi: doi.org/10.1029/2012TC003206.

Mayor, J., Calvet, M., Margerin, L., Vanderhaeghe, O. & Traversa, P., 2016. Crustal structure of the Alps as seen by attenuation tomography, *Earth planet. Sci. Lett,* **439,** 71–80.

Meier, T., Soomro, R.A., Viereck, L., Lebedev, S., Behrmann, J.H., Weidle, C., Cristiano, L. & Hanemann, R., 2016. Mesozoic and cenozoic evolution of the Central European lithosphere, *Tectonophysics,* **692,** 58–73.

Mitchell, B., 1995. Anelastic structure and evolution of the continental crust and upper mantle from seismic surface wave attenuation, *Rev. Geophys Space Phys.,* **33,** 441–462.

Mroczek, S., Tilmann, F., Pleuger, J., Yuan, X. & Heit, B. SWATH-D Working Group, AlpArray Working Group, 2023, Investigating the Eastern Alpine-dinaric transition with teleseismic receiver functions: evidence for subducted European crust, *Earth planet. Sci. Lett.,* **609,** 118096. doi: 10.1016/j.epsl.2023.118096.

Napolitano, F., De Siena, L., Gervasi, A., Guerra, I., Scarpa, R. & La Rocca, M., 2020. Scattering and absorption imaging of a highly fractured fluid-filled seismogenetic volume in a region of slow deformation, *Geosci. Front.,* **11,** 989–998.

Nardoni, C., De Siena, L., Cammarano, F., Magrini, F. & Mattei, E., 2021. Modelling regional-scale attenuation across Italy and the Tyrrhenian Sea, *Phys. Earth Planet.,* **318,** 106764. doi: 10.1016/j.pepi.2021.106764.

Nardoni, C., De Siena, L., Magrini, F., Cammarano, F., Maeda, T. & Mattei, E., 2023. Earthquake characteristics and structural properties of the Southern Tyrrhenian Basin from full seismic wave simulations, *Surv. Geophys.,* **44,** 925–945.

Neubauer, F., 2003. Geology of Europe, *Encyclopedia of Life Supporting Systems,* eds: De Vivo, B., Grasemann, B. & Stüwe, K., UNESCO Publishing Eolss Publishers, Oxford, UK.

Oancea, V., Bazacliu, O. & Mihalache, G., 1991. Estimation of the coda quality factor for the Romanian territory, *Phys. Earth Planet.,* **67**(1–2), 87–94.

Oncescu, M.C. & Bonjer, K.P., 1997. A note on the depth recurrence and strain release of large Vrancea earthquakes, *Tectonophysics,* **272,** 291–302.

Oros, E., Placinta, A.O. & Moldovan, I.A., 2021. Seismicity, active stress pattern and fault reactivation potential in South Carpathians, *Rom. J. Phys.,* **66,** 811. https://rjp.nipne.ro/2021_66_9-10.htm.

Padhy, S., 2009. Characteristics of body-wave attenuations in the Bhuj crust, *Bull. seism. Soc. Am.,* **99**(6), 3300–3313.

Paraschiv, D. 1979. Platforma Moesică şi Zăcămintele Ei de Hidrocarburi. Editura Academiei, Bucureşti, 195pp (in romanian).

Pécskay, Z. *et al.*, 2006. Geochronology of Neogene magmatism in the Carpathian arc and intra-Carpathian area: a review, *Geol. Carpathica,* **57**(6), 511–530.

Petrescu, L., Borleanu, F., Kästle, E., Stephenson, R., Plăcintă, A. & Liashchuk, O.I., 2023b. Seismic structure of the Eastern European crust and upper mantle from probabilistic ambient noise tomography, *Gondwana Res.,* **125,** 390–405.

Petrescu, L., Borleanu, F. & Placintă, A.O., 2022. Seismic structure of a Tethyan back-arc: trans-dimensional ambient noise tomography of the Black Sea lithosphere, *Phys. Earth Planet.,* **325,** 106854. doi: 10.1016/j.pepi.2022.106854.

Petrescu, L., Borleanu, F., Radulian, M., Ismail-Zadeh, A. & Maţenco, L., 2021. Tectonic regimes and stress patterns in the Vrancea Seismic Zone: insights into intermediate-depth earthquake nests in locked collisional settings, *Tectonophysics,* **799,** 228688. doi: 10.1016/j.tecto.2020.228688.

Petrescu, L., Plăcintă, A.O., Borleanu, F., Radulian, M. & Cioflan, C.O., 2023a. Past earthquake simulations using ambient seismic noise in Vrancea, Romania, *Seismol. Res. Lett.,* **94**(5), 2373–2383.

Petrescu, L., Stuart, G., Tataru, D. & Grecu, B., 2019. Crustal structure of the Carpathian Orogen in Romania from receiver functions and ambient noise tomography: how craton collision, subduction and detachment affect the crust, *Geophys. J. Int.,* **218,** 163–178.

Pharaoh, T.C., 1999. Palaeozoic terranes and their lithospheric boundaries within the Trans-European Suture Zone (TESZ): a review, *Tectonophysics,* **314,** 17–41.

Pharaoh, T.C., Winchester, J.A., Verniers, J., Lassen, A. & Seghedi, A., 2006. The western accretionary margin of the east European Craton: an overview, *Mem. Geol. Soc. Lond.,* **32**(1), 291–311.

Placintă, A.O., Borleanu, F., Popescu, E., Radulian, M. & Munteanu, I., 2021. Earthquake source properties of a lower crust sequence and associated seismicity perturbation in the SE Carpathians, Romania, collisional setting, *Acoustics,* **3,** 270–296.

Poli, P., Pedersen, H.A. & Campillo, M., 2012. Emergence of body waves from cross-correlation of short period seismic noise, *Geophys. J. Int.,* **188**(2), 549–558.

Popa, M., Andreea, C., Raluca, D., Cristian, C., Bogdan, G. & Borleanu, F., 2022. Romanian earthquake catalogue (ROMPLUS). *Mendeley Data,* V2, doi:10.17632/tdfb4fgghy.2.

Popa, M., Munteanu, I., Borleanu, F., Oros, E., Radulian, M. & Dinu, C., 2018. Active tectonic deformation and associated earthquakes: a case study – South West Carpathians Bend Zone, *Acta Geod. Geophys.,* **53,** 395–413.

Priyono, A. *et al.*, 2021. Seismic attenuation tomography of the 2018 Lombok, Indonesia, earthquake aftershocks, *Front. Earth Sci.,* **9**. doi: 10.3389/feart.2021.639692.

Radulian, M., Bala, A. & Toma-Danila, D., 2020. Refmc 1929 - 2012 (Romanian Earthquake Focal Mechanism Catalogue). *Mendeley Data,* V3, doi:10.17632/mykkx4gygy.3.

Radulian, M., Mândrescu, N., Panza, G.F. & Utale, A., 2000. Characterization of seismogenic zones of Romania, *Pure appl. Geophys.,* **157,** 57.

Răileanu, V., Diaconescu, C. & Rădulescu, F., 1994. Characteristics of Romanian lithosphere from deep seismic reflection profiling, *Tectonophysics,* **239,** 165–185.

Rawlinson, N., Fichtner, A., Sambridge, M. & Young, M.K., 2014. Seismic tomography and the assessment of uncertainty, *Adv. Geophys.,* **55,** 1–76.

Rawlinson, N. & Spakman, W., 2016. On the use of sensitivity tests in seismic tomography, *Geophys. J. Int.,* **205,** 1221–1243.

Ren, Y., Grecu, B., Stuart, G.W., Houseman, G.A. & Hegedüs, E. South Carpathian Project Working Group, 2013. Crustal structure of the carpathian–Pannonian region from ambient noise tomography, *Geophys. J. Int.,* **195**(2), 1351–1369.

Ren, Y., Stuart, G.W., Houseman, G.A., Dando, B., Ionescu, C., Hegedüs, E., Radovanović, S. & Shen, Y. South Carpathian Project Working Group, 2012. Upper mantle structures beneath the carpathian-pannonian region, implications for the geodynamics of continental collision, *Earth planet. Sci. Lett.,* **349–350,** 139–152.

Sanborn, C.J., Cormier, V.F. & Fitzpatrick, M., 2017. Combined effects of deterministic and statistical structure on high-frequency regional seismograms, *Geophys. J. Int.,* **210,** 1143–1159.

Sato, H., Fehler, M.C. & Maeda, T., 2012. *Seismic Wave Propagation and Scattering in the Heterogeneous Earth,* Second edn, Springer, Berlin.

Schaefer, J.F., Boschi, L. & Kissling, E., 2011. Adaptively parametrized surface wave tomography: methodology and a new model of the European upper mantle: adaptively parametrized surface wave tomography, *Geophys. J. Int.,* **186,** 1431–1453.

Schmid, S.M. *et al.*, 2008. The Alpine-carpathian-dinaridic orogenic system: correlation and evolution of tectonic units, *Swiss J. Geosci.,***101,** 139–183.

Seghedi, A., Vaida, M., Iordan, M. & Verniers, J.C.L., 2005. Paleozoic evolution of the Romanian part of the Moesian platform: an overview, *Geol. Belgica,* **8/4,** 99–120 84.

Seghedi, I. *et al.*, 2019. Tectono-magmatic characteristics of post-collisional magmatism: case study East Carpathians, Călimani Gurghiu-Harghita volcanic range, *Phys. Earth Planet.,* **293,** 106270. doi: 10.1016/j.pepi.2019.106270.

Seghedi, I., Ntaos, T., Pécskay, Z., Panaiotu, C., Mirea, V. & Downes, H., 2022. Miocene extension and magma generation in the Apuseni Mts. (western Romania): a review, *Int. Geol. Rev.,* **64**(13), 1885–1911.

Shapiro, S.A., Schwarz, R. & Gold, N., 1996. The effect of random isotropic inhomogeneities on the phase velocity of seismic waves, *Geophys. J. Int.,* **127**(3), 783–794.

Sketsiou, P., Napolitano, F., Zenonos, A. & De Siena, L., 2020. New insights into seismic absorption imaging, *Phys. Earth Planet,* **298,** 106337. doi: 10.1016/j.pepi.2019.106337.

Soergel, D., Pedersen, H.A., Stehly, L., Margerin, L. & Paul, A. AlpArray Working Group, 2020. Coda-Q in the 2.5–20 s period band from seismic noise: application to the greater Alpine area, *Geophys. J. Int.,* **220**(1), 202–217.

Sokolov, V.Y., Wenzel, F. & Mohindra, R., 2008. Probabilistic seismic hazard assessment for Romania and sensitivity analysis: a case of joint consideration of intermediate-depth (Vrancea) and shallow (crustal) seismicity, *Soil Dyn. Earthq., Eng.,* **29,** 364–381.

Souriau, A. *et al.*, 2011. Multimethod characterization of the French-pyrenean valley of Bagnères-de-Bigorre for seismic-hazard evaluation: observations and models, *Bull. seism. Soc. Am.,* **101,** 1912–1937.

Stipčević, J., Herak, M., Molinari, I., Dasović, I., Tkalčić, H. & Gosar, A., 2020. Crustal thickness beneath the Dinarides and surrounding areas from receiver functions, *Tectonics,* **39**(3), https://doi.org/10.1029/2019TC005872.

Szanyi, G., Gráczer, Z., Balázs, B. & Kovács, I.J. AlpArray Working Group, 2021. The transition zone between the Eastern Alps and the Pannonian basin imaged by ambient noise tomography, *Tectonophysics,* **805,** 228770. doi: 10.1016/j.tecto.2021.228770.

Takahashi, T., Sato, H., Nishimura, T. & Obara, K., 2007. Strong inhomogeneity beneath quaternary volcanoes, revealed from the peak delay analysis of S-wave seismograms of microearthquakes in northeastern Japan, *Geophys. J. Int.,* **168**(1), 90–99.

Tărăpoancă, M., Bertotti, G., Maţenco, L., Dinu, C. & Cloetingh, S.A.P.L., 2003. Architecture of the Focşani depression: a 13 km deep basin in the Carpathians Bend Zone (Romania). *Tectonics,* **22,** 1074. doi: 10.1029/2002TC001486.

Tari, G.C. & Horváth, F., 1995. Middle Miocene extensional collapse in the Alpine-Pannonian transition zone, pp. 75–105, *Hungary: Extensional Collapse of the Alpine Orogen and Hydrocarbon Prospects in the Basement and Basin Fill of the Western Pannonian Basin,* eds: Horváth, F., Tari, G. & Bokor, Cs, AAPG International Conference and Exhibition, 10-13 September Nice, 6th Field Trip Notes Hungary.

Thybo, H., Pharaoh, T. & Guterch, A., 2002. Geophysical Investigations of the Trans European Suture Zone II, introduction, *Tectonophysics,* **360,** 1–4.

Tiliţă, M., Lenkey, L., Maţenco, L., Horváth, F. & Dinu, C., 2006. Neogene evolution of Transylvanian basin: insights derived from (2D steady-state) thermal modeling. *Geophysical Research Abstracts,* European Geosciences Union General Assembly 2006, Vienna, Austria, 2-7 April 2006, **8,** 08874. SRef-ID: 1607-7962/gra/EGU06-A-08874.

Ustaszewski, K., Schmid, S.M., Fügenschuh, B., Tischler, M., Kissling, E. & Spakman, W., 2008. A map-view restoration of the Alpine–Carpathian–Dinaridic system for the early Miocene, *Swiss J. Geosci.,* **101**(1), 273 –294.

Văcăreanu, R., Radulian, M., Iancovici, M., Pavel, F. & Neagu, C., 2015. Fore-arc and back-arc ground motion prediction model for Vrancea intermediate depth seismic source, *J. Earthq. Eng.,* **19,** 535–562.

van der Hoeven, A.G.A. *et al.*, 2005. Observation of present-day tectonic motions in the south-eastern Carpathians: geodetic results of the ISES/CRC-461 GPS measurements, *Earth planet. Sci. Lett,* **239**(3–4), 177–184.

Visarion, M. & Veliciu, S., 1981. Some geological and geophysical characteristics of the Transylvanian Basin, *Earth Evol. Sci.,* **3-4,** 212–217.

Wéber, Z., 2002. Imaging Pn velocities beneath the Pannonian basin, *Phys. Earth planet. Inter.,* **129,** 283–300.

Wessel, P., Smith, W.H.F., Scharroo, R., Luis, J. & Wobbe, F., 2013. Generic mapping tools: improved version released, *EOS Trans. Am. geophys. Un.,* **94**(45), 409–410.

Wilde-Piorko, M. *et al.*, 2008. PASSEQ 2006-2008: passive seismic experiment in Trans-european Suture Zone, *Stud. Geophys. Geod.,* **52,** 439–448.

Yang, Y., Liu, C. & Langston, C., 2020. Processing seismic ambient noise data with the continuous wavelet transform to obtain reliable empirical Green's functions, *Geophys. J. Int.,* **222**(2), 1224 –1235.

Yoshimoto, K., Sato, H. & Ohtake, M., 1993. Frequency-dependent attenuation of P and S waves in the Kanto area, Japan, based on the coda-normalization method, *Geophys. J. Int.,* **114**(1), 165–174.

Zhao, D., Kanamori, H., Negishi, H. & Wiens, D., 1996. Tomography of the source area of the 1995 Kobe earthquake: evidence for fluids at the hypocenter?. *Science,* **274**(5294), 1891–1894.